



Effect of partial and global shielding on surface-driven phenomena in keyhole mode laser beam welding

Leander Schmidt¹ · Klaus Schrickler¹ · Christian Diegel¹ · Florian Sachs¹ · Jean Pierre Bergmann¹ · Andrea Knauer² · Henry Romanus² · Herwig Requardt³ · Yunhui Chen^{3,4} · Alexander Rack³

Received: 18 July 2023 / Accepted: 4 November 2023 / Published online: 1 December 2023
© The Author(s) 2023, corrected publication 2023

Abstract

Partial shielding by means of local gas supply has proven to be very effective in reducing spatter. Besides the effect of gas-induced dynamic pressure, the shielding of oxygen is also highly relevant for melt pool dynamics and spatter formation due to the growth of oxides and the influence on surface tension. Therefore, this paper addresses the effect of local supplied argon on oxide growth and seam topography during keyhole mode laser beam welding of high-alloy steel AISI 304. To determine the shielding quality, the results are compared to laser beam welding in a global argon atmosphere. The topography of the upper weld seams was analyzed by scanning electron microscopy (SEM). An X-ray microanalysis (EDX) in line scan modus was performed to determine and to locate the elements which are covering the specimen surface. The chemical state of the found elements was quantified by X-ray photoelectron spectroscopy (XPS). In a last step, high-speed synchrotron X-ray imaging was performed to separate the effect of the gas-induced pressure and the gas-induced shielding on keyhole geometry. The results show that a local supply of argon contributes to a significant difference in oxide growth, affecting melt pool convection and weld seam geometry. It was further shown that the effect of gas flows at low flow rates is primarily because of oxygen shielding, as no significant difference in keyhole geometry was found by high-speed synchrotron X-ray imaging.

Keywords Laser beam welding · Spatter formation · Oxide formation · Melt pool dynamics · Gas atmosphere

1 Introduction

Spatter formation is a major challenge in high-speed laser beam welding, especially when welding high-alloy steels. The process is initiated when the sum of the metal vapor induced kinetic energy E_{vap} and the kinetic energy of the

fluid element $E_{\text{kin,fl}}$ is equal to or greater than the sum of the kinetic energy of the spatter $E_{\text{kin,sp}}$ and the surface energy of the melt E_{sur} (Eq. 1) [1].

$$E_{\text{vap}} + \underbrace{\rho V_{\text{sp}} v_{\text{fl}}^2}_{E_{\text{kin,fl}}} = \underbrace{\rho V_{\text{sp}} v_{\text{sp}}^2}_{E_{\text{kin,sp}}} + \underbrace{2\sigma S_{\text{sp}}}_{E_{\text{sur}}} \quad (1)$$

Partial shielding in the form of locally supplied gas has proven to be very effective in reducing spatter formation, e.g. for partial penetration welding of high-alloy steels with welding speeds of 1 m/min [2], 1.5–5 m/min [3, 4], 6 m/min [5] and even at high welding speeds up to 16 m/min [6, 7]. The spatter reduction was also observed during welding of full penetration welding of high-alloy steel up to 16 m/min [8], while the spatter-induced loss of mass could be reduced up to 70%. Due to the massive reduction in spatter formation, the specimen surface was largely free of spatter adhesion, while the top of the seam was often observed to be locally widened [6]. As a result of affected spatter trajectories, detached spatters were re-absorbed into the downstream melt pool [8]. In addition, the formation of

Recommended for publication by Commission IV - Power Beam Processes

✉ Leander Schmidt
leander.schmidt@tu-ilmenau.de

¹ Production Technology Group, Technische Universität Ilmenau, Gustav-Kirchhoff-Platz 2, 98693 Ilmenau, Germany

² Center of Micro- and Nanotechnologies (ZMN), Gustav-Kirchhoff-Straße 7, 98693 Ilmenau, Germany

³ ESRF – The European Synchrotron, Structure of Materials Group - ID19, F-38043 Grenoble Cedex 9, France

⁴ School of Engineering, RMIT University, Melbourne, Australia

a more circular keyhole aperture was observed, while the melt pool was prolonged due to the local gas supply [7]. The changes in spatter formation and melt pool dynamics were mainly attributed due to the effect of the gas flow on the pressure balance of the keyhole, which gives the ratio of keyhole-opening to keyhole-closing pressures (Eq. 2) according to [9, 10].

$$p_{\text{recoil}} + \Delta p_{\text{dp}_v} = p_{\sigma} + p_h + p_{\text{dyn}}; \Delta p_{\text{dp}_v} = p_v - p_0 \quad (2)$$

The pressure balance includes the physical quantities of p_{recoil} as recoil pressure, Δp_{dp_v} as differential vapor pressure, p_{σ} as surface tension pressure, p_h as hydrostatic pressure, p_{dyn} as hydrodynamic pressure, p_v as vapor pressure and p_0 as atmospheric pressure. Up to now, the influence of the gas flow-induced dynamic pressure p_{gas} has been preferred to attribute the fundamental effect mechanism by increasing the keyhole-opening pressures (Eq. 2) [8, 11], which can be approximated by Eq. 3 including ρ_{gas} as gas density and v_{gas} as gas flow velocity.

$$p_{\text{gas}} = 1/2 \cdot \rho_{\text{gas}} \cdot v_{\text{gas}}^2 \quad (3)$$

Since recent results have shown that the melt pool dynamics and spatter formation can differ dependent on the used shielding gas (Ar, N, He), while the flow rates were adapted for reaching similar dynamics pressures (normalization), the effect of partial shielding by means of a local gas supply cannot be solely attributed to the influence of dynamic pressure [12].

Following, it is necessary to consider other possible determinants. In literature, it is well known that the gas atmosphere has a significant effect on the formation of welding imperfections (e.g. spatter and pore formation) [13, 14], melt pool dynamics [15] and resulting weld seam geometry [16, 17]. In particular, the shielding of oxygen through the use of inert gases has a strong influence on the melt pool dynamics, since the oxygen concentration is highly relevant for the growth of a specimen covering top layer (e.g. oxides) [18].

The process of oxide growth can be classified into two parts in general. Based on the high-temperature laser welding process, molecular oxygen dissociates into highly reactive atomic oxygen [19]. Subsequently, the atomic oxygen present in the atmosphere next to the welding zone reacts with the metal or alloying element that is present at the interface between the metal and the gas, depending on temperature and partial pressure [20, 21]. Oxide nuclei are formed at this interface and grow during the transient phase of the reaction until a first layer is formed [22]. The gradient of chemical potentials is essential for a further oxide growth since the formed layer represents a gas/oxygen barrier [23]. Consequently, any further oxide growth is based on solid-state diffusion, which depends on the structure of the crystal

and the grain boundaries [22]. Because the initial formation of the oxide layer is much faster than the subsequent diffusion-based process, the growth rate decreases over time. The oxide layer thickness s_{Ox} can be calculated by the parabolic rate law (Eq. 4), including the temperature-dependent parabolic rate constant k_p and growth time t [24].

$$s_{\text{Ox}}^2 = k_p' \cdot t \quad (4)$$

The region in which the oxide layer grows depends on the diffusion velocities of the ions and electrons. If the oxygen anions in the oxide layer can move faster than the metal cations, the oxide layer grows from the inner side of the metal-oxide interface (e.g. Fe_2O_3 , SiO_2 , TiO_2). If the metal cations in the oxide layer can move faster than the oxygen anions, the oxide layer grows from the outside at the oxide-gas interface (e.g. Cr_2O_3 , FeO , NiO , Cu_2O). If the ions in the oxide layer can move faster than the electrons, both cases can occur (e.g. Al_2O_3) [19]. Since technical applications often use alloys, which usually consist of a large number of chemical elements (e.g. AISI 304), the growth mechanism can act in parallel.

The formation of oxides affects the melt pool convection since the layer causes a shear-induced deceleration of near-surface melt flows, particularly in the case of Marangoni convection [25]. Thus, the magnitude of the Marangoni convection is related to the presence and growth of oxides [26]. Since the flow direction of the Marangoni convection depends on the temperature-dependent gradient of the surface tension [27] which is positive for liquid iron with an oxygen content greater or equal than approx. 0.009 wt% [28], the Marangoni flow is directed from the weld seam edge to the weld seam centre (centripetal) when welding in ambient atmosphere [15]. However, the surface tension gradient becomes negative for oxygen contents less than or equal to approx. 0.0017 wt% in liquid iron [28], which means that a shielding of oxygen can cause an inversion of the flow direction [15, 17]. As a result, the melt flows from the centre of the weld to the edge of the weld (centrifugal), causing a local widening of the weld seam top when welding in an inert gas atmosphere [14, 16]. Nevertheless, it should be noted that the temperature coefficient can change its positive or negative sign depending on the temperature and the concentration of surfactants [29]. This can result in an inversion of the Marangoni convection during the welding process. It should also be noted that the effect of the Marangoni convection decreases with an increase in welding speed [9, 30], making it particularly relevant for lower welding speeds [1] as well as for TIG welding [31].

The change in surface tension can also affect the formation of spatter. According to the condition of spatter formation (Eq. 1), the critical energy for spatter

detachment is related to the surface tension. In the case of welding iron, an oxygen shielding causes an increase in surface tension [32], which can result in a decrease of spatter formation by enhancing the critical energy for spatter detachment.

Consequently, it can be concluded that the atmosphere has a significant influence on the melt pool dynamics and spatter formation by affecting the growth of oxides and manipulating the surface tension. Therefore, this study is concerned with the effect of locally supplied argon on the surface morphology and topography of AISI 304 during keyhole laser beam welding in continuation of the previously studied effect of the gas-induced dynamic pressure. To characterize the shielding quality, the results are compared to laser beam welding in a global argon atmosphere. High-speed synchrotron X-ray imaging was performed to separate the effect of the gas-induced pressure and the oxygen shielding on keyhole geometry and keyhole fluctuations in addition.

2 Materials and methods

2.1 Experimental welding setup

Bead-on-plate welds were performed on 2-mm-thick specimens of stainless austenitic steel AISI 304 (X5CrNi18-10, 1.4301) using a disk laser (Trumpf TruDisk 5000.75, $P_{max} = 5 \text{ kW}$, $\lambda = 1030 \text{ nm}$). Two different experimental setups were used for realizing a global gas atmosphere and a partial shield by means of a local gas supply. In both experimental setups, the laser beam was in focus at the specimen surface. A remote laser scanning system (Scanlab intelliWELD 30 FC) was utilized to weld fixed samples in a global gas atmosphere (Fig. 1a). For investigating the effect of a local gas supply (Fig. 1b), the specimens were handled by a six-axis robot (Kuka KR 60HA) and welded by using a stationary arranged welding optics (Trumpf BEO D70). The robot speed v_m was inverse to the welding speed v_w . Technical specifications of the used setups are given in Table 1.

Fig. 1 Experimental environments. **a** Setup for global gas atmosphere. **b** Setup for local gas supply

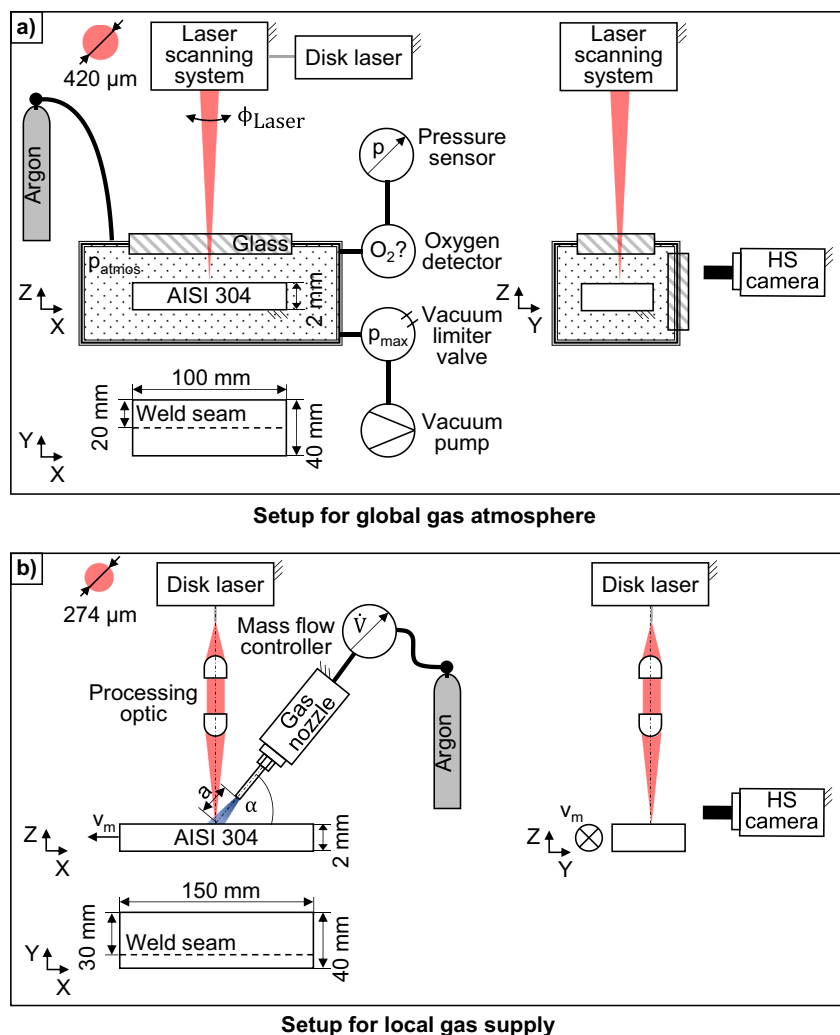


Table 1 Technical specifications and used parameters

Laser optics	P_L	d_{foc}	v_m	Specimen handling	Specimen environment
Setup 1: Welding in a global gas atmosphere					
Remote laser scanning system	3.5 kW	420 μm	8 m/min	Fixed position	Welding chamber
Setup 2: Welding with local gas supply					
Stationary welding optics	2.18 kW	274 μm	10 m/min	Six-axis robot	Local gas supply in atmosphere

To compensate the difference in focal diameter of both setups ($d_{\text{foc}} = 420 \mu\text{m}/274 \mu\text{m}$), the weld parameters (laser power, welding speed) were adjusted for each setup to provide comparable characteristics of the welding processes (criteria: similar melt pool dynamics and spatter formation). Section 3.2 provides a detailed description of the process characteristics for each setup.

To set up the global gas atmosphere (Fig. 1a), the welding chamber was evacuated with a vacuum pump in a first step. The vacuum was limited to $p_{\text{chamber}} \geq 200$ mbar by using a vacuum limiter valve (Schmalz VR-G1/4-IG) to avoid possible damage of the chamber. After the evacuation, argon 5.0 was fed in to restore ambient pressure. The argon 5.0 used was in accordance with ISO 14175:2008 and had a purity of 99.999%. The procedure was repeated until an oxygen concentration < 20 ppm was reached, checked by using an oxygen sensor (Erika Jankus JAero F). The pressure inside the chamber was monitored during the procedure and the welding process by a pressure sensor (Thermovac TTR 101). The protection windows of the chamber were made of borosilicate glass (Schott BOROFLOAT®33) to minimize the optical loss during the transmission of the laser beam into the chamber (transmittance about 93% for $\lambda = 1030$ nm). For the experiments with local gas supply (Fig. 1b), a custom gas nozzle unit, described in detail in [6], was mounted to the stationary welding optics. The gas nozzle was set to a trailing flow orientation with a flow angle of $\varphi = 48^\circ$ and a nozzle distance of $a = 5$ mm, feeding argon 5.0 at a flow rate of $V = 2$ l/min, based on the parameter set for achieving best weld results (lowest spatter formation, defect-free surface) of [6–8]. The nozzle had an inner diameter of 1.4 mm. The flow rate was controlled by a mass flow controller (Bronkhorst FG-201AV-AGD-33-V-D A-000). A high-speed camera (Photron SA-X2) equipped with a zoom lens (Navitar 12X Zoom Lens System) was used in both setups for a process recording at 10,000 frames per second. The camera was set in parallel to the specimen surface to record melt pool dynamics and spatter formation. A narrow-band filter with a centre wavelength of 808 nm was used to mask out process emissions. To quantify the effect of spatter formation on the loss of material, the specimens were weighed before and after the welding process using a high-precision balance (Kern PLJ 2000-3A).

Based on the captured high-speed video data, the amount of spatter was counted by visual inspection using the full image sequence.

2.2 High-speed synchrotron X-ray imaging

High-speed synchrotron X-ray imaging was performed at the European Synchrotron Radiation Facility (ESRF) at Beamline ID19 (Fig. 2). AISI 304 with a thickness of 3 mm was used and penetrated by an X-ray beam of $4 \times 4 \text{ mm}^2$ with an energy ≤ 60 keV. The scintillator material used was Ce-doped $\text{Lu}_3\text{Al}_5\text{O}_{12}$ with a thickness of 250 μm from manufacturer Crytur, lens-coupled to a Photron SA-Z high-speed camera (propagation distance 4.5 m, framerate 40,000 Hz). For more information on the theory of high-speed synchrotron X-ray imaging, see [33]. A spatial resolution of 4 μm per pixel was achieved within the high-speed recordings. Image processing was performed to reduce artifacts in the image and to increase the contrast between the keyhole and the surrounding material as well as between the melt pool and the atmosphere. A processed image F_n was calculated where n is the index of an individual image, I_n is an indexed frame from the high-speed recording and \bar{I} is an average image of 100 frames recorded with the sample moving at

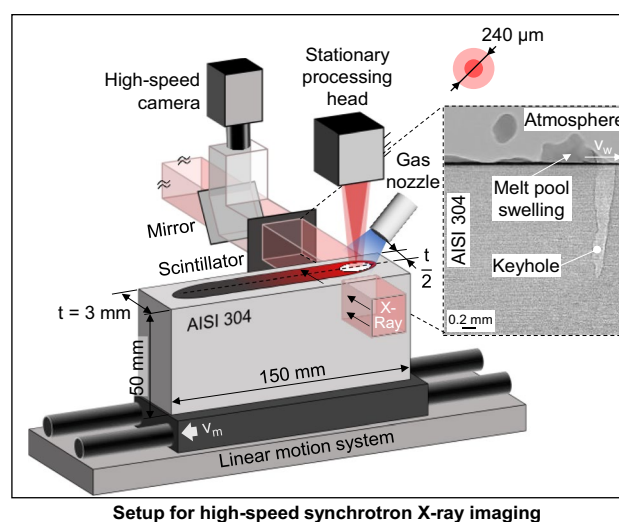


Fig. 2 Experimental setup for high-speed synchrotron X-ray imaging with local gas supply

the welding speed but without carrying out the laser welding process (Eq. 5).

$$F_n = \frac{I_n}{I} \quad (5)$$

Stack images were created based on 1000 sequential frames using the minimum intensity projection feature of Fiji [34]. Afterwards, the brightness was normalized for each image, reaching a maximum grey value of 170 (8-bit grey value image). For increasing the comprehensibility, the black and white images were converted to false colour images by using the “physics” look-up table of Fiji. For the welding process, a fiber laser (Coherent HighLight FL8000-ARM) and a stationary welding optics (Precitec YW52) was used. The specimen was handled by a linear motion system (three-axis linear motion system, isel). The core power (P_{core}) to ring power (P_{ring}) of the laser system ($d_{\text{foc}} = 240 \mu\text{m}$) was set to a calculated top-hat intensity distribution to ensure a high comparability of all used welding setups. Gas was supplied with the same setup and nozzle as described in Section 2.1.

2.3 Material analysis

A surface morphological analysis of the specimen was carried out using two different scanning electron microscopes (Table 2).

To identify the elements which are covering the surface and their chemical state, a XPS investigation were carried out using a SPECS SAGE HR 150 system equipped with a 1D delayline detector using monochromatized AlK α radiation (excitation energy $h\nu = 1486.7 \text{ eV}$) and the analyzer Phoibos 150. The calibration of the energy scale was ensured by reference measurements on a polycrystalline silver sample. The measurements were carried out after 20 min of sputtering with argon plasma to remove the utmost of unwanted adventitious hydrocarbons from the surface (acceleration voltage for sputtering: 3 kV; argon pressure: $2.2 \cdot 10^{-3} \text{ mbar}$). An energy-dispersive X-ray spectroscopy (EDX) in line scan mode with a Bruker EDX Quantax 200 Z30 detector was also performed to increase the spatial resolution of the chemical elemental analysis. The acceleration voltage was set to 20 kV with a working distance of 7 mm,

Table 2 Specifications of SEM analysis

SEM system	Working distance	Accelerating distance
Hitachi S-4800	8.4 mm	11 kV
ZEISS GeminiSEM 300	7.5 mm	20 kV

resulting in an excitation area of approximately $d_{x/y} = 8 \mu\text{m}$ (surface area), $d_z = 4 \mu\text{m}$ (penetration depth). All element analyses were performed on unetched specimens.

3 Experimental results

3.1 Effect of local gas supply on keyhole formation

Since the state of the art focuses primarily on surface-related phenomena (e.g. effects on spatter formation and near-surface melt pool dynamics), no information with high temporal and spatial resolution is available on keyhole formation and dynamics of keyhole mode laser beam welding processes using comparable settings of laser power and welding speed. Therefore, high-speed synchrotron X-ray imaging was performed for visualizing the keyhole formation and dynamics of the non-gas-assisted process (reference process) and the keyhole behaviour of the gas-assisted process. Beginning with the gas-unaffected reference process (Fig. 3a), the formation of a keyhole with a narrow aspect ratio (ratio of keyhole length to depth) and a highly stable keyhole front was observed. A fluctuating bulge of the bottom of the keyhole was found, which did not collapse. The keyhole depth was constant throughout the entire welding process. The rear wall of the keyhole was fluctuating with high frequency. While the lower part of the keyhole rear wall was fluctuating with lower amplitude, the upper part showed a higher fluctuation amplitude. These fluctuations contributed to the formation of spatter, which can be characterized by four different sub-steps (Fig. 3a, I–IV). In the first step (Fig. 3a, I), a fluctuating melt pool swelling was formed at the upper keyhole rear wall. After 0.2 ms (Fig. 3a, II), the melt pool swelling was transformed into a melt column due to the upward momentum of the melt pool. A further upward movement caused a necking of the melt column within another 0.2 ms (Fig. 3a, III). In a last step, the spatter was separated from the melt pool (Fig. 3a, IV). By realizing a partial shielding using a local gas supply (Fig. 3b), a notable change in spatter formation could be observed. While the first frames in the series show the formation of an upward rising melt pool swelling on the upper keyhole rear wall also (Fig. 3b, I, II), the keyhole and melt pool dynamics of the gas-assisted process often did not lead to spatter formation. Instead of a spatter detachment, the height of the melt pool swelling increased, and the melt was fed back into the downstream melt pool by the formation of a reverse melt flow (Fig. 3b, II–IV). The local gas supply had also an effect on the stability of the keyhole bottom. While the reference process (Fig. 3a) was characterized by a stable keyhole bottom, a pore separation could be detected by using locally supplied gas. Beginning with the formation of a keyhole bulging in the initial frames of the series (Fig. 3b, V), pores were separated at

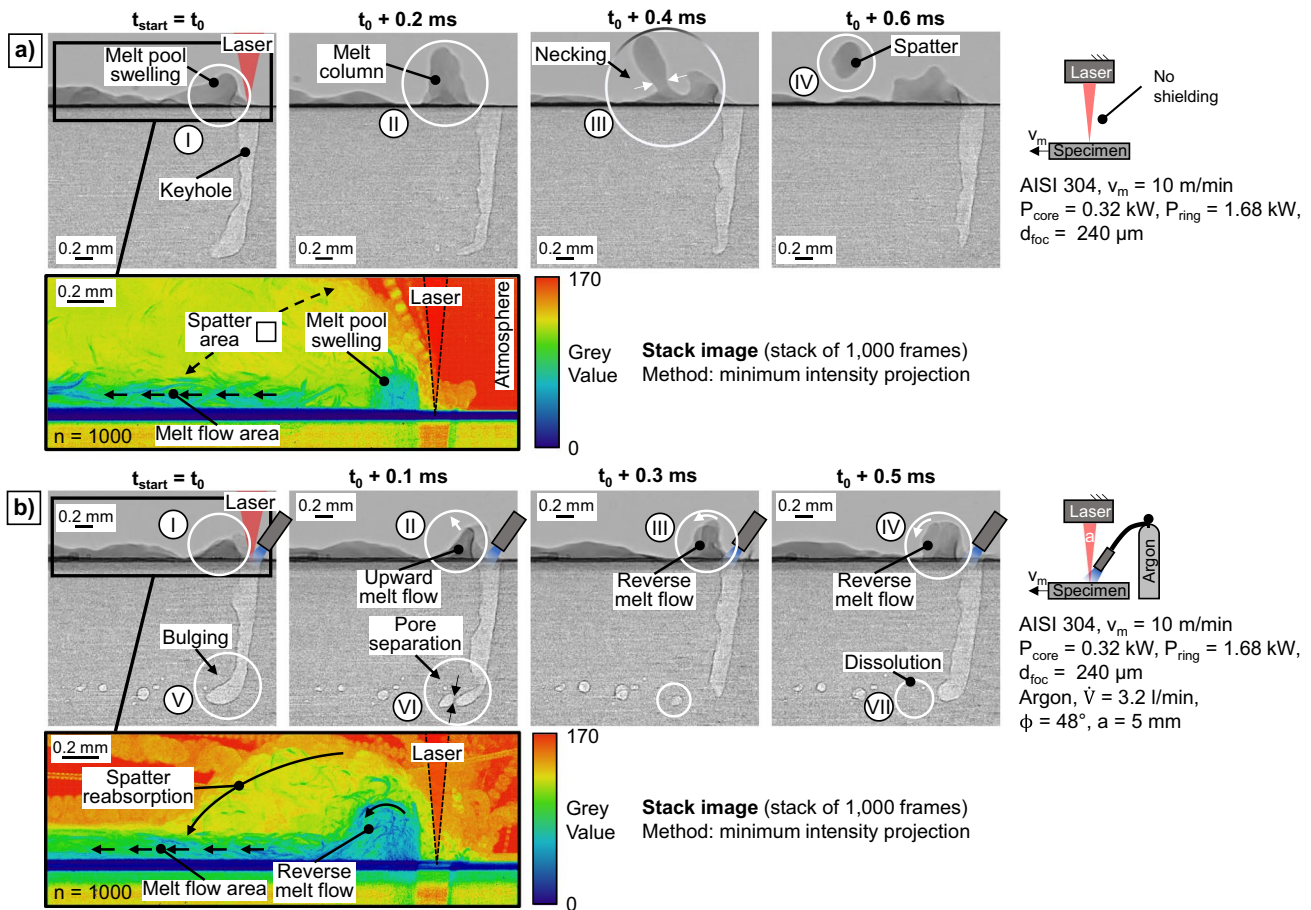


Fig. 3 High-speed synchrotron X-ray imaging: **a** reference process. **b** local supply of argon

the keyhole tip within another 0.1 ms (Fig. 3b, VI). In some cases, pores were observed to be dissolving (Fig. 3b, VII), which can be explained by the condensation of metal vapor inside the cavity according to [35]. However, it was not possible to observe any further gas-induced changes in keyhole geometry and keyhole dynamics by visual inspection, while the formation of spatter changed significantly. In order to attribute these changes, the video data was further processed to provide false colour images. Therefore, stack images of 1000 sequential frames are provided for each setup (reference/gas-assisted). Based on the chosen projection method (Section 2.2) and the difference in grey value of the solid material (e.g. melt pool) to the X-ray image background, the grey values of the stack images indicate the distribution of spatter and the melt pool geometry over time. By analyzing the stack image of the reference process (Fig. 3a), a large-sized spatter area (■) was found, indicating spatter trajectories in the opposite of the weld direction. Furthermore, the formation of the melt pool swelling at the keyhole rear wall followed by a melt flow area was observed. Based on the high-speed recordings, a flow direction against welding direction can be attributed to this melt flow area. In contrast

to the reference process, the stack image of the gas-assisted process (Fig. 3b) illustrates the formation of a significant higher melt pool swelling. Next to this, a melt flow area was formed. By using the local gas supply, a smaller spatter area was found. While the most spatter trajectories of the reference process exceeding the field of view of the X-ray recordings, the spatter trajectories of the gas-assisted process indicate a spatter reabsorption into the downstream melt pool. This can be attributed to a significant lower kinetic energy of the detached spatter. Since no significant change in keyhole geometry and keyhole dynamics was found for the gas-assisted process (except for pore formation at the keyhole tip), the difference in spatter formation and melt pool dynamics must be strongly influenced by some physical effect other than the gas-induced pressure [12]. In this context, the use of non-reactive gases (inert gases) can affect the melt pool dynamics by a change in surface tension and oxide growth due to a shielding of oxygen. To investigate the effect of coverage, the following sections provide an overview of the effect of partial shielding by means of a local gas supply on the chemical composition of the weld seam and their topological structure. To characterize the coverage of

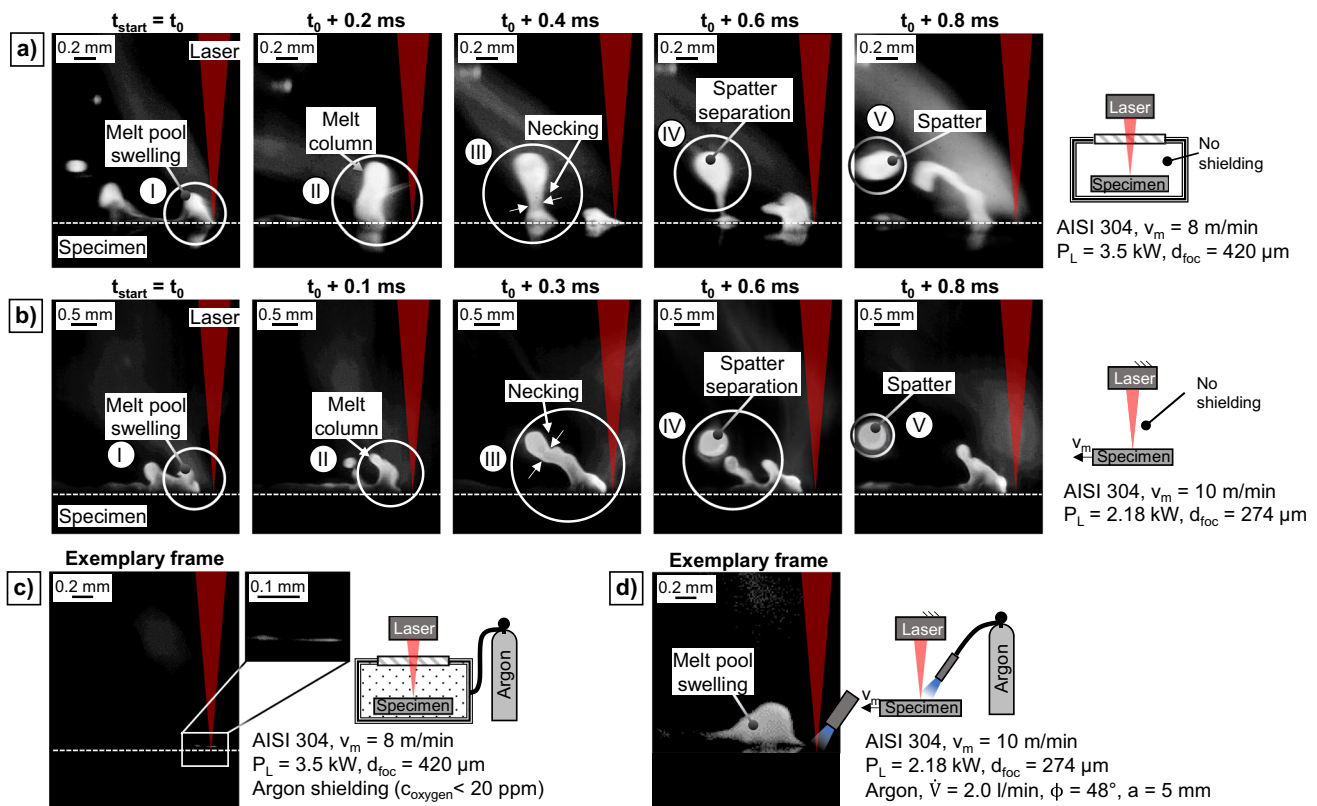


Fig. 4 High-speed recordings of the melt pool dynamics and spatter formation: **a** ambient atmosphere in a process chamber, **b** ambient atmosphere, **c** argon atmosphere in process chamber and **d** locally supplied argon

locally supplied gas, the experiments are compared to weld experiments in a global gas atmosphere.

3.2 Effect of partial and global shielding on melt pool dynamics and spatter formation

The following section focuses on the comparison of the melt pool dynamics and spatter formation of welding processes realized with global and partial shielding (Fig. 4). Since the focal diameter of both setups (global atmosphere/local gas supply) was different (Section 2.1), the process parameters (laser power, welding speed) were adapted to ensure comparable spatter formation mechanism and the same penetration depth (approx. 1.7 mm). To demonstrate the effect of the parameter adaption, Fig. 4 a and b show the upper melt pool dynamics for the reference processes of both environmental setups (ambient atmosphere inside the process chamber (Fig. 4a), welding in atmosphere without locally supplied gas (Fig. 4b)). The comparison of the high-speed recordings revealed similar melt pool characteristics for both setups, which can be attributed to the single wave regime according to [36]. Accordingly, the frame series of both reference processes (Fig. 4a, b) illustrate a nearly identical sequence of spatter formation. The initial frames show the formation of

a melt pool swelling at the upper keyhole rear wall (Fig. 4a, b, I), followed by a transformation of this melt pool swelling into a melt column (Fig. 4a, b, II). Afterwards, a necking of this melt column could be observed (Fig. 4a, b, III) before the spatter was separated (Fig. 4a, b, IV) and eject out of the melt pool (Fig. 4a, b, V). Since the melt pool dynamics for both reference processes can be considered comparable, it can be concluded that, despite the differences in focal diameter, the parameter adaption provides a reasonable basis for comparing the effect of a partial and global shielding.

As the effect of locally supplied argon on spatter formation and melt pool dynamics has already been described in Section 3.1, the effect of a global argon atmosphere (Fig. 4c) is referred to there. For a visual comparison of both effects, Fig. 4d shows again the effect of locally supplied argon. By changing the ambient gas atmosphere into a global argon atmosphere inside the process chamber, a significant change in melt pool dynamics and spatter formation was observed (Fig. 4c). While the reference processes (Fig. 4a, b) and the local gas-assisted process (Fig. 4c) resulted in the formation of a pronounced melt pool swelling, the use of a global argon atmosphere induced only a small melt pool swelling, which was barely visible on the upper surface (Fig. 4c). Furthermore, a significant reduction in spatter formation could be

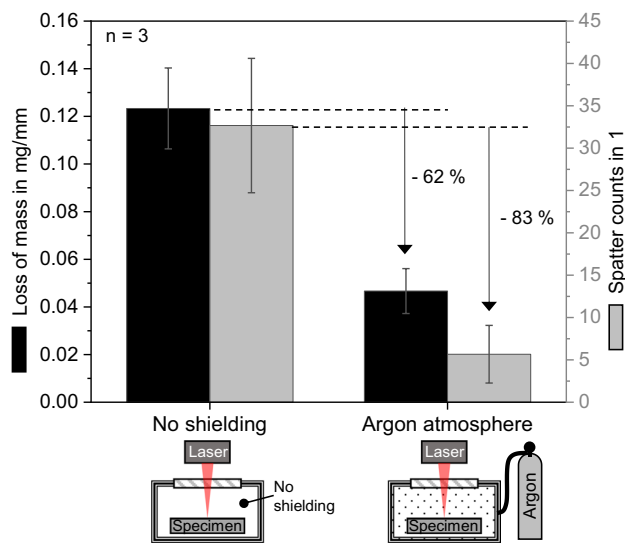


Fig. 5 Loss of mass and spatter counts for laser beam welding in a global gas atmosphere

observed. Since the reduction in the spatter-induced loss of mass of the local gas-assisted process is already described in [6–8], Fig. 5 provides the loss of mass and the spatter counts depending on a global gas atmosphere (ambient/argon). By using the global argon atmosphere, a reduction in the loss of mass of 62% was achieved, while the spatter counts were reduced by 83% in an almost similar wise. Since preliminary investigations determined a nearly identical reduction in the loss of mass of up to 91% by using locally supplied argon (e.g. [6]), the oxygen shielding seems to have a significant effect, especially when feeding argon at low flow rates (approx. up to 5 l/min), resulting in low dynamics pressures. An increase in chamber pressure due to thermal expansion of the material and ambient gas is neglected since the pressure monitoring during the experiments proved a constant pressure inside the chamber (Section 2.2). As the main effect of the shielding of oxygen can be given by a change in oxide growth as well as an affected surface tension, the absence of oxygen can influence the weld seam geometry and topography due to an affected melt pool convection. Therefore, the following section examines the effect on weld seam cross sections and specimen top sides.

3.3 Effect of partial and global shielding on weld seam geometry and weld seam topography

By analyzing metallographic cross sections of the weld seams, a significant difference in weld seam geometry (Fig. 6a) and surface quality (Fig. 6b) was found. While the specimen top sides of the reference processes of both setups were characterized by spatter adhesion and partial seam undercuts (Fig. 6b), a defect-free and almost

spatter-free surface was observed for welding with partial and global shielding, except for the formation of melt protuberances on the weld seam edge of the specimens welded in the global argon atmosphere. As melt protuberances are formed by a laterally ejected and non-separated melt column [37] and this paper is focussed on spatter formed at the keyhole rear wall, the formation of melt protuberances will therefore not be discussed further. The coverage of argon also resulted in a local widening of the weld seam top ($\Delta w_{\text{seam}}^{\text{local}} = +19\%$, $\Delta w_{\text{seam}}^{\text{global}} = +41\%$). This is typical for a change in Marangoni convection and is usually followed by a decrease in penetration depth (e.g. [15]), as has been observed in the global gas atmosphere ($\Delta z_{\text{pen}} = -28\%$). In contrast, a local supply of argon resulted in a slight increase in penetration depth ($\Delta z_{\text{pen}} = +10\%$), which was already noticed for a higher welding speed ($v_w = 12$ m/min) and attributed to a change in energy deposition in [6]. Another difference between the effect of the partial and global shielding was found with respect to the formation of tarnish. While the specimen welded in the global argon atmosphere was free of tarnish, all other specimens showed dark-coloured tarnish formation. Although the general effects of the partial and global shielding are mostly identical, this implies differences in the coverage, which can affect the oxide growth and thus influencing the magnitude of the melt pool convection. Therefore, the following section is focused on the determination of the surface covering elements and their chemical state by XPS analysis. It should be noted that due to the 1 mm diameter measuring spot, the XPS analysis area partially covered the base material depending on the weld seam width, especially for the specimen welded with locally supplied argon (Fig. 6c). This results in a measurement deviation, which is considered in the following discussion of the results.

3.4 Effect of partial and global shielding on the composition and the chemical state of surface elements

Figure 7a gives an example of an XPS survey spectrum taken from a specimen welded in a global argon atmosphere, showing the characteristic secondary electron peaks, Auger lines (KLL, LMM) and the valence band (VB) of the contained elements. By summing up the $2p_{3/2}$ secondary electron peaks, the total element concentration of the specimens was determined (Fig. 7b) according to [38]. Since the chemical composition of AISI 304, according to the DIN EN 10088-3 standard, is an average over the thickness of the sheet and can differ particularly in the area near the surface, a non-welded sample was also analyzed to provide a surface-related reference spectrum. This measurement is depicted as reference in the following graphs.

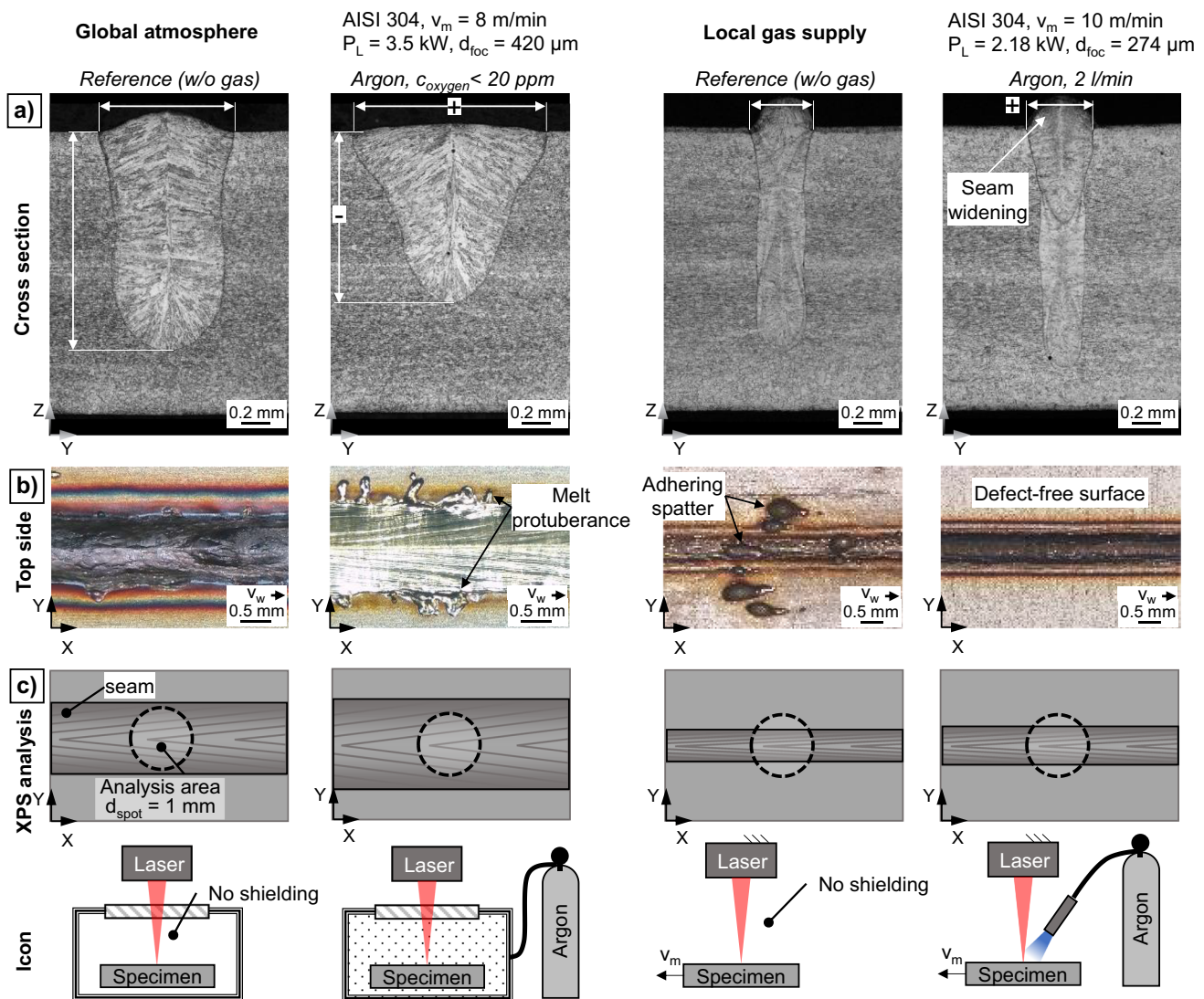


Fig. 6 Comparison of the effect of global and partial shielding on weld seam formation: **a** cross sections, **b** specimen top sides, **c** true to scale analysis area of XPS analysis

By comparing the measured element concentrations of the specimen surface (Fig. 7b), a high amount of oxygen was found (approx. 20–27 at.%), which can be attributed to the XPS information which is limited to the first 2 nm of the surface due to the small mean free path of electrons in solids [39]. As a result, the XPS measurement is particularly subjected to surface-active processes (e.g. oxidation). In general, all welded samples contained a higher amount of oxygen and carbon, while the amount of iron, chromium and nickel was decreased compared to the non-welded sample. This can be attributed to a change in the ratio of elements, whereby the significant increase in oxygen and carbon results in a decrease in all other elements. By comparing the effect of the gas atmosphere, ambient-welded specimens showed an increase in manganese, chromium (only for the reference process of the local gas supply) and silicon,

which is consistent with the thermodynamic calculations of [25] that indicated an increase in iron, manganese, chromium and silicon oxides for GTA-welded specimens of SUS 304 in an ambient atmosphere with an oxygen concentration of more than 0.6 vol%. To specify whether the increase in the element concentration can be attributed to the growth of oxides, the following discussion focuses on the determination of the chemical states. Since the elemental concentration of silicon is comparatively low, the determination is concentrated on the oxidation states of iron (Fig. 8a), chromium (Fig. 8b) and manganese (Fig. 8c). The corresponding high-resolution XPS spectra (Fig. 20, Fig. 21, Fig. 22, Fig. 23, Fig. 24, Fig. 25) are included in the Appendix as the further discussion is based on a quantitative comparison.

A decrease of elemental iron (Fe-0) was observed for all welded specimen (Fig. 8a), while the amount of Fe-II

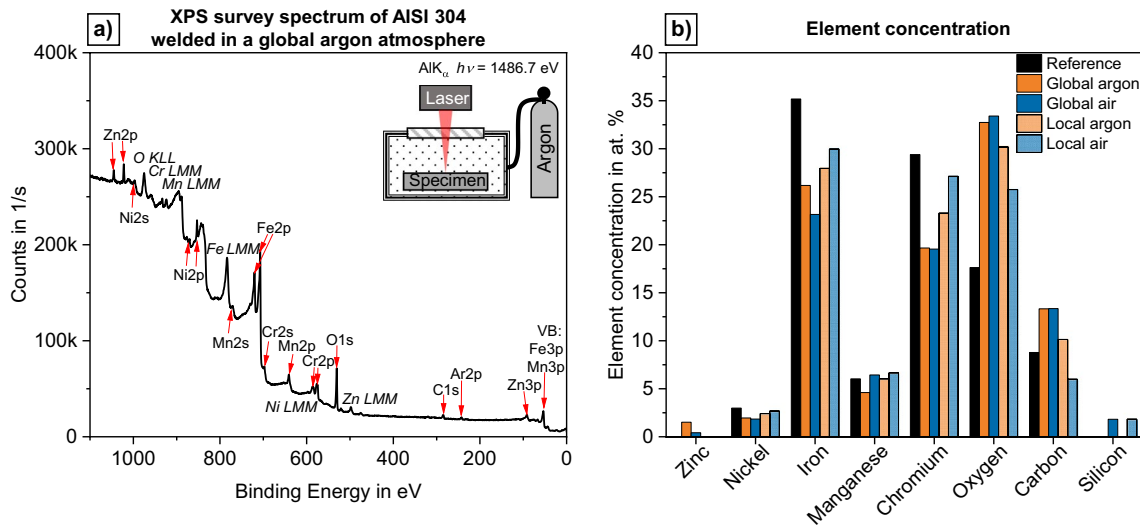


Fig. 7 (a) XPS survey spectrum of AISI 304 welded in global argon atmosphere; (b) element concentration determined by XPS analysis for partially and globally shielded welded specimen and a non-welded specimen (reference)

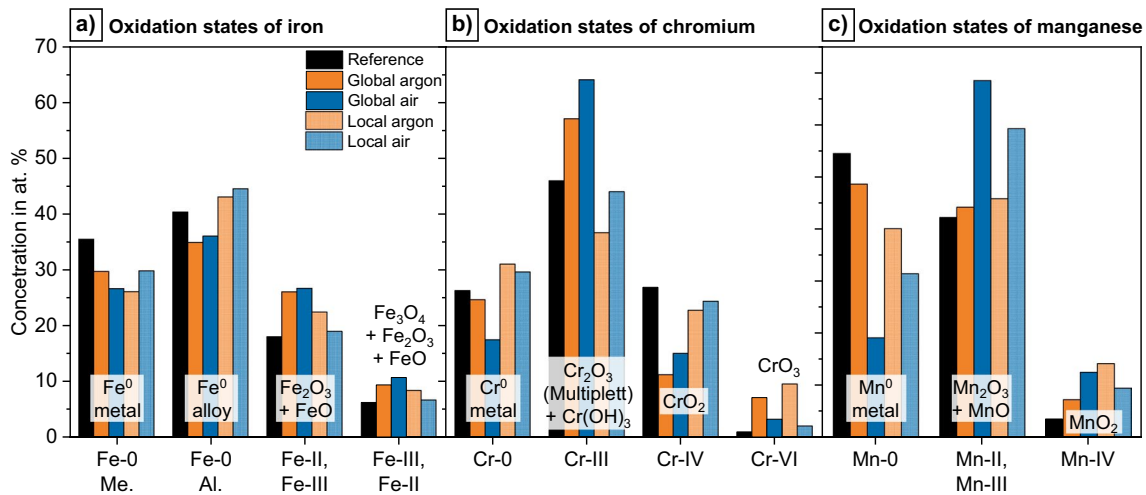


Fig. 8 Oxidation states determined by XPS analysis: **a** iron, **b** chromium and **c** manganese

and Fe-III states increased at the same time. Despite a slight increase in Fe-0 (alloy) was observed for all specimen welded in an ambient atmosphere too, the increase in Fe-II and Fe-III states indicates the formation of iron oxide on the specimen surface because of the welding process. However, a trend in the amount of Fe-II and Fe-III states as a function of type of shielding (partial/global) could not be determined. In contrast, the analysis of the oxidation states of chromium (Fig. 8b) and manganese (Fig. 8c) showed more similarities. Thus, all samples welded in ambient atmosphere showed a decrease of elemental chromium (Cr-0), elemental manganese (Mn-0) and Cr-VI

state, while at the same time a significant increase of Cr-III, Cr-IV and Mn-II, Mn-III states could be detected. This corresponds to a significant increase in chromium oxides and manganese oxides on the specimen surface, while the surface is also covered by iron oxides. To identify the geometrical structure, spatial distribution and layer thicknesses of these oxides, the following section provides a surface analysis of the specimen using a scanning electron microscope (SEM) and energy-dispersive X-ray spectroscopy (EDX) in line scan mode. To emphasize the effect of the gas atmosphere in a more explicit way, this section is divided into Subsections 3.5 (Effect of partial and global shielding) and 3.6 (Effect of ambient atmosphere).

3.5 Effect of partial and global shielding on oxide growth and spatial element distribution

To provide a representation of the effect of an ideal argon shielding, the discussion will first focus on the effect of a global argon atmosphere. By analyzing the cross section of the specimen (Fig. 9), a seam formation without covering oxide layer was observed. This corresponds to the EDX measurement of the chemical concentration (Fig. 10). The line scan began approximately 100 μm inside the weld seam, crossed the area of the specimen surface and ended outside the specimen. By analyzing the concentration of carbon (C), oxygen (O), silicon (Si), chromium (Cr), manganese (Mn), iron (Fe) and nickel (Ni), a homogeneous elemental

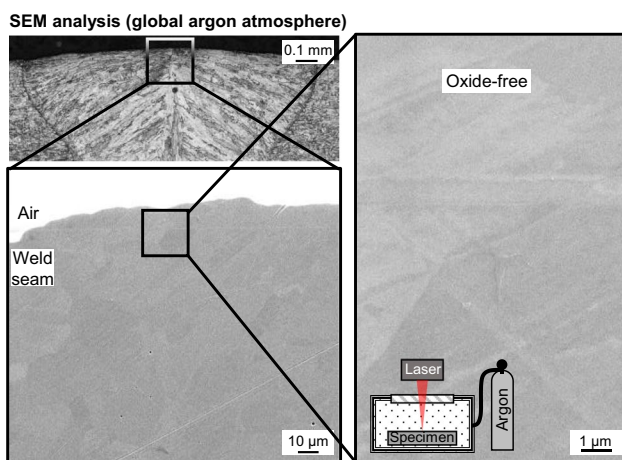


Fig. 9 Microstructure of AISI 304 welded in a global argon atmosphere

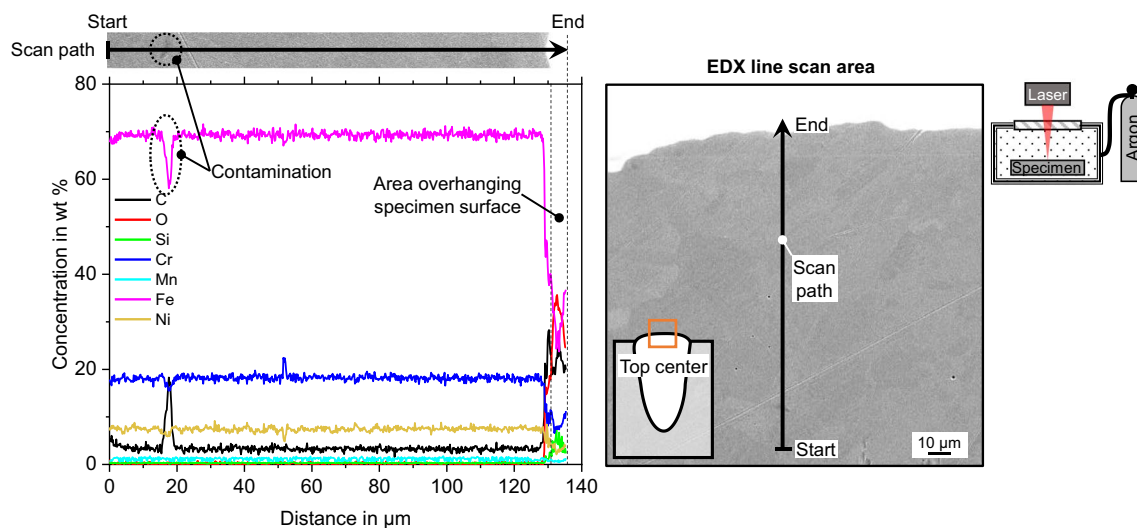


Fig. 10 Element concentration determined by EDX analysis of a specimen welded in a global argon atmosphere

distribution was found along the entire scan path. This leads to the conclusion that the oxide growth in a global argon atmosphere is weak due to the inert nature of the gas, which could already be determined based on the differences in the tarnish formation (Fig. 6). Following, the oxides determined by surface-sensitive XPS analysis are limited to layer thicknesses below the resolution limit of the SEM analysis (reached max. SEM resolution: 14.3 nm/px) and the detection limit of the EDX analysis (set EDX line scan resolution: 50 nm/point). Since the weld geometry of the global argon atmosphere-welded specimen was characterized by an extensive widening of the weld top (Section 3.2), the thin oxides present on the top of the specimen can be considered of minor importance with respect to a surface-near melt pool convection.

The SEM analysis of the specimen welded with locally supplied argon revealed an almost comparable weld seam (Fig. 11). Thus, it was not possible to detect an all-over covering oxide layer in the near-surface area. However, a few areas of formed clusters were found at the edge of the seam. To specify the chemical elements within these structures, a line scan was performed across and along this area (Fig. 12). While the area next to the cluster showed no differences in chemical composition (Fig. 12, I), a decrease in iron and nickel and an increase in oxygen, manganese, silicon and carbon were detected within the cluster (Fig. 12, II). This is consistent with the XPS measurement, which revealed an increase in the chemical state of manganese and silicon (Section 3.4), among others, suggesting that the locally formed clusters can be related to oxide islands composed mainly of oxidized manganese and silicon. Consequently, the results imply an imperfect coverage of the locally supplied gas,

SEM analysis (local argon supply)

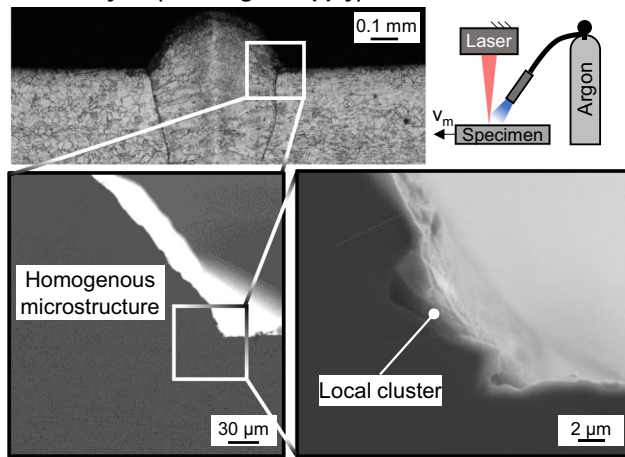


Fig. 11 Microstructure of AISI 304 welded with locally supplied argon

resulting in an occasional contact between the melt and ambient oxygen. From an industrial point of view, manganese and silicon are often used in the steelmaking process as deoxidizers to increase slag formation [40], which is probably relevant to the redistribution of chemical elements during the welding process and may be related to the formed oxide islands.

In order to identify possible areas of oxide clusters, Fig. 13 shows an EDX line scan across the top of the specimen. In addition, the corresponding surface topography is shown by an SEM analysis to investigate the correlation between the spatial element distribution and the surface topography. Using the local argon supply, a widely homogeneous distribution of elements was observed on

the specimen top side. However, a decrease in iron and nickel and an increase in manganese, oxygen and silicon were determined in a few local areas across the width of the seam. By correlating the corresponding surface topography, it was found that these areas were located on local maxima in the chevron ripples of the seam (Fig. 13, D). The uneven topography of the ripples may influence the EDX analysis by affecting the excitation area. Nevertheless, due to the high spatial resolution of the EDX analysis (Section 2.3), this effect can be considered of minor importance. According to the XPS analysis (Section 3.4), these areas may consist of oxidized manganese and silicon. Since the formation of the chevron structure depends significantly on the interaction of different melt flows within the melt pool [41], the spatial distribution of these locally thickened oxide layers seems to be affected by the melt pool convection. In this context, the melt pool convection caused the formation of an almost symmetrical chevron structure (Fig. 13, Detail A), with less symmetry in the edge regions of the seam. Although the EDX analysis revealed the formation of local oxide islands, the surface of the chevron ripples was free of spalling oxides (Fig. 13, Detail B).

In summary, a partial shielding by means of a local gas supply can largely prevent the formation of oxides. However, there can be occasional contact between the melt and oxygen, allowing for potential oxide formation.

3.6 Effect of an ambient atmosphere on oxide growth and spatial element distribution

In addition to the oxygen concentration within the atmosphere, the growth of oxides is also dependent on temperature and time [19]. To investigate this dependency more

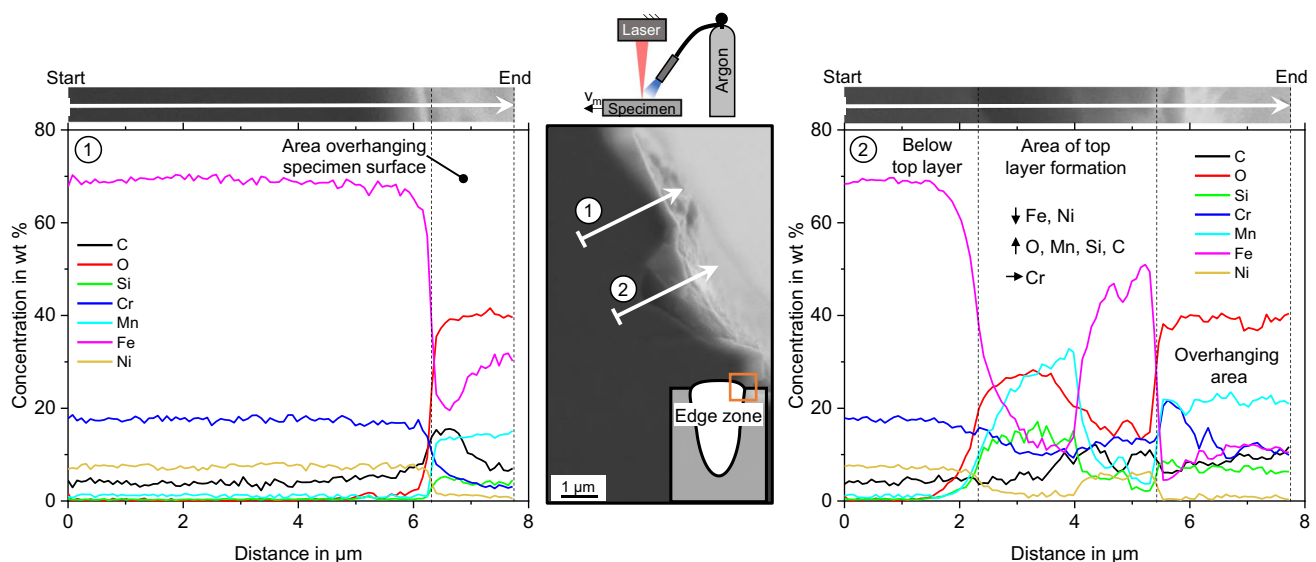


Fig. 12 Element concentration determined by EDX analysis of a specimen welded with locally supplied argon

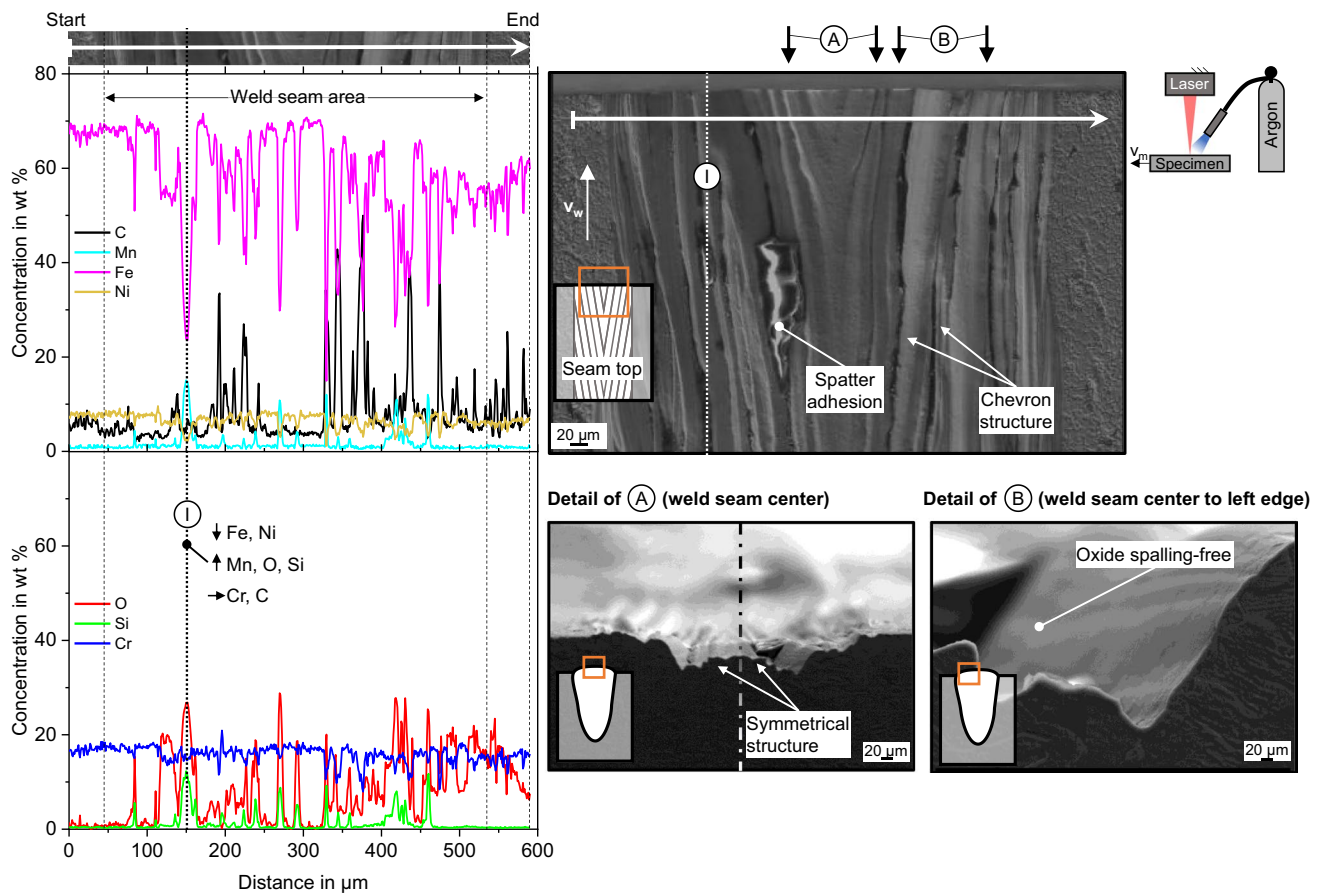


Fig. 13 Surface topography and spatial element distribution of AISI 304 welded with locally supplied argon

explicit, the following analysis of the oxide growth in ambient atmosphere is performed for both experimental setups (Section 2.1), since the used welding speeds and focal diameter (global atmosphere: $v_m = 8$ m/min, $d_{foc} = 420$ μm , local gas supply: $v_m = 10$ m/min, $d_{foc} = 274$ μm) are different and could therefore influence the oxide growth.

By analyzing the chamber-welded specimen in ambient atmosphere, a significant change in the seam formation was noted compared to the specimen welded in a global argon atmosphere (Fig. 14). The surface was characterized by an all-over covering top layer, the thickness of which varied depending on the spatial seam position. With a thickness of approx. 500 nm, the layer was thinnest in the centre of the weld seam and increased up to approx. 8 μm towards the edge of the seam. The thickness of the layer did not grow consistently, whereby especially the edge area showed strong variations in layer thickness. Inside this layer, cubical structures were found stacked on top of each other. While the smaller cubical structures were settled in the lower part of the covering top layer, the largest structures were concentrated on the upper side. These structures were embedded in a lamellar matrix that seems to consist of at least two chemical elements, based on the difference in SEM contrast.

To determine the chemical composition of the covering top layer, Fig. 15 provides a spatially resolved EDX line scan. Beginning in the material below the top layer, a high concentration of iron, chromium and nickel was found. By crossing the top layer formation, a significant increase in oxygen, chromium, manganese and silicon was detected. This agrees with the XPS analysis (Section 3.4) and indicates the formation of chromium oxides, manganese oxides and silicon oxides within the top layer; in addition, the surface-sensitive XPS analysis also indicates the formation of iron oxides.

To give a representation of the layer structure, it might be useful to consider the oxidation kinetics. Since the region in which the oxide layer grows can be different (Section 1), the oxide layer can consist of a multilayer structure. According to this, the growth reaction of Cr_2O_3 and FeO , among others, causes to the formation of the outer oxide layer, while Fe_2O_3 and SiO_2 , among others, grows from the inner to the outer layer [19]. This can explain the differences in the spatial element distribution within the oxide layer, as shown in the EDX line scan in Fig. 15. Corresponding to this, it was possible to identify an increase in silicon within the embedding matrix material surrounding the cubical structures (Fig. 15,

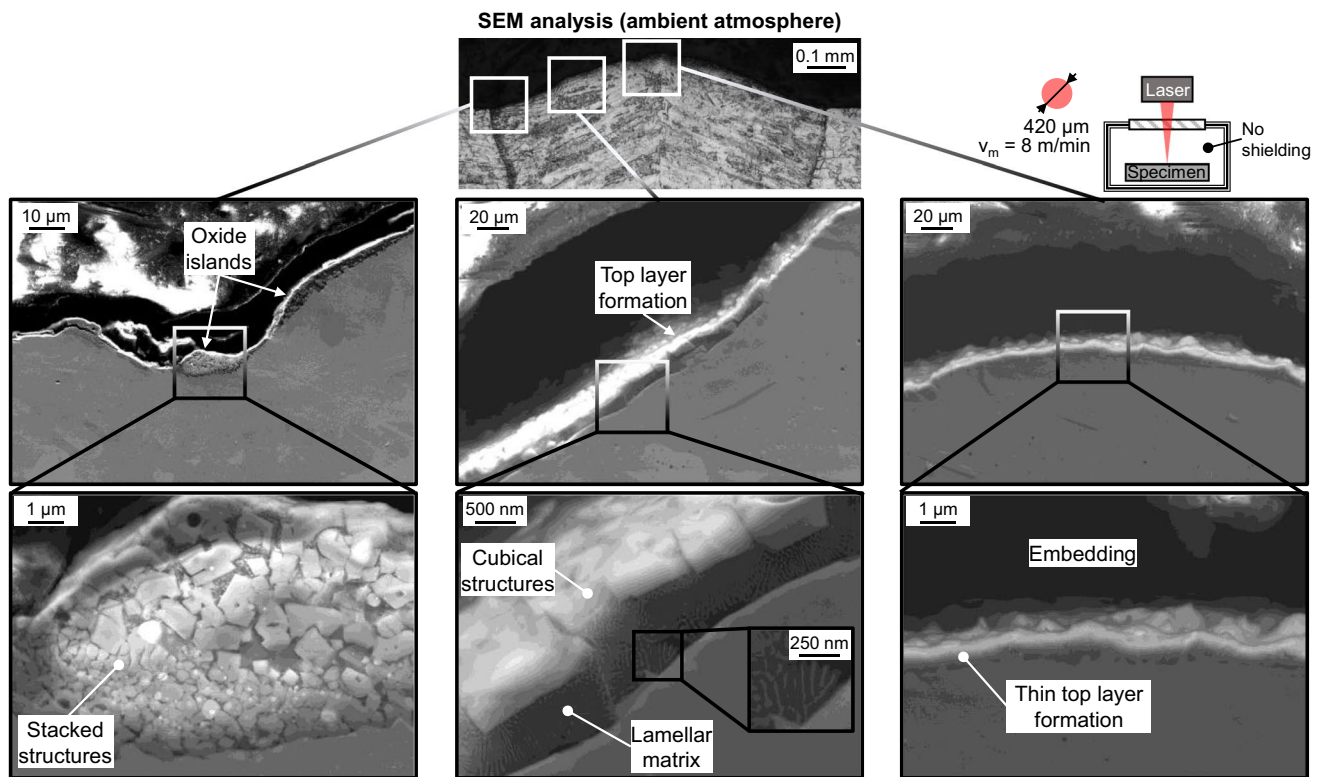


Fig. 14 Microstructure of AISI 304 welded in a chamber at ambient atmosphere

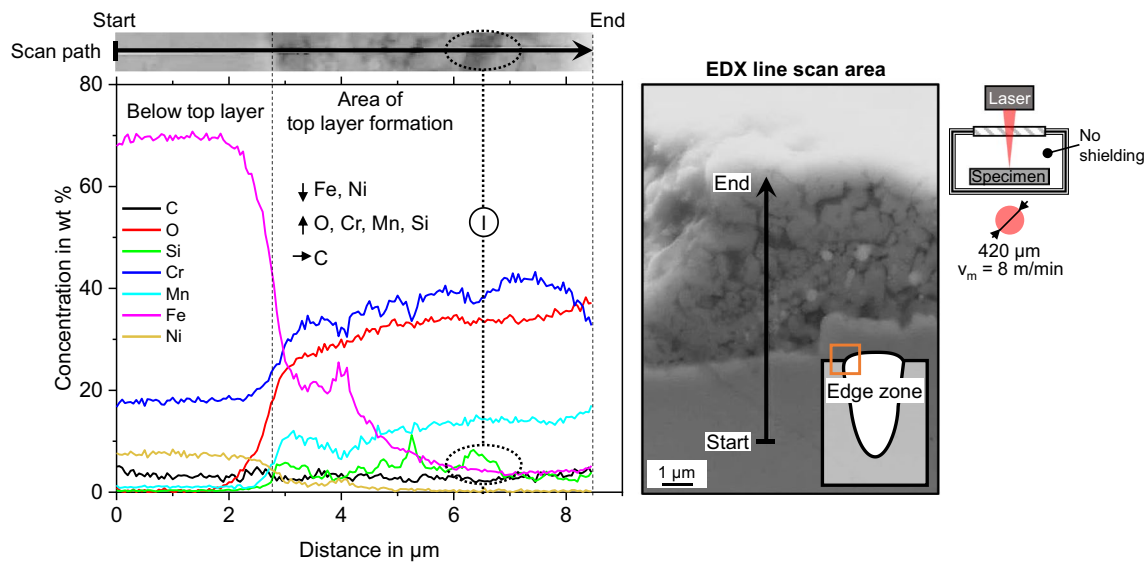


Fig. 15 Element concentration determined by EDX analysis of AISI 304 welded in a chamber at ambient atmosphere

I), which can be a result of the inner growth of SiO_2 . The formation of the cubical structures can be attributed to two different phenomena. Since the formed volume of the oxides is usually larger than the volume of the initial metal from which the oxide is created, the oxide growth results in the

formation of compressive stress within the formed layer [42]. This ratio is given by the Pilling-Bedworth ratio (P-B ratio). As the P-B ratio of most of the oxidation-relevant elements of AISI 304 is greater than 1 (e.g. Fe(II) oxide: 1.7, Cr(III) oxide: 2.07, Fe(II,III) oxide 2.10 and SiO_2 : 2.15), the

oxide layer tends to form cracks [19], which may be crucial for the formation of the cubical structures within the seam. The second formation mechanism can be attributed to the melt pool convection. Following, the melt flow during the welding process may break up the formed oxide layer and can also result in a redistribution of oxides on the weld seam surface. This could explain the stacks of the cubical structures in the edge of the seam. Since the temperature gradient of the surface tension of liquid iron should be positive for welding processes in ambient atmosphere (Section 1), the centripetal melt flow direction of the melt contradicts this theory. Therefore, it can be assumed that the resultant of the keyhole surrounding flow, the metal vapor induced flow and the Marangoni flow contribute to the weld seam edge-orientated redistribution of oxides. Since the velocity

of the keyhole surrounding melt flow increases exponentially with welding speed [1, 9, 30], and the experiment was performed at relatively high welding speeds (Section 2.1), the redistribution of the oxides may be dominated by the effect of the keyhole surrounding melt flow.

By increasing the welding speed and decreasing the focal diameter for the chamberless-welded specimen in ambient atmosphere, an almost comparable oxide formation was observed (Fig. 16). An all-over covering top layer was observed, while the seam edge was characterized by localized increases in layer thickness/cluster as described above. However, the general thickness of the top layer was significantly thinner than that of the chamber-welded specimen. This may be attributed to the differences in welding parameters (Section 2.1), following the increase in welding speed and decrease in focal diameter results in a faster seam solidification, reducing the time of interaction between oxygen and melt. In addition, the melt pool convection, and therefore the distribution of oxides, is affected by the increase in welding speed. The layer thickness can also increase after solidification. However, this influence is to be considered minor since the adsorption is temperature dependent (Section 1). To determine the chemical elements in the top layer, another EDX line scan was performed (Fig. 17). Inside the thickened areas at the seam edge (Fig. 17, I), a decrease in iron and nickel and an increase in manganese, oxygen, silicon and carbon were found, while the concentration of chromium remained constant. Except for the constant chromium concentration, this corresponds to the found element concentration on the chamber-welded specimen. An almost similar behaviour was noticed in the area next to the thickened layer (Fig. 17, II). In this case, a decrease in iron, chromium and nickel and an increase in oxygen, manganese, silicon and especially carbon were observed. Despite the differences

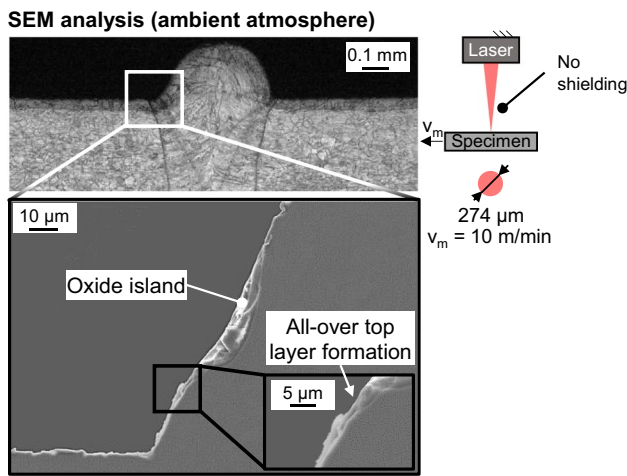


Fig. 16 Microstructure of AISI 304 welded chamberless in ambient atmosphere

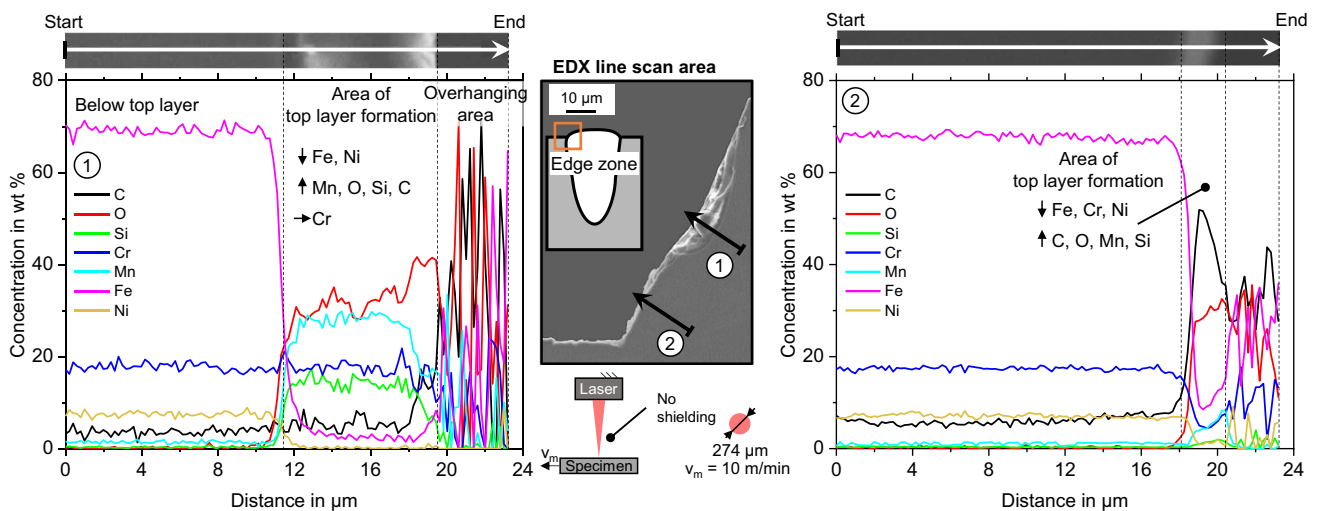


Fig. 17 Element concentration determined by EDX analysis of AISI 304 welded chamberless at ambient atmosphere

in the total element concentration between both measuring sites, the trend of the curves is mostly the same. Considering the XPS analysis (Section 3.4), it can be assumed that the top layer of the chamberless-welded specimen consists mainly of oxidized manganese and silicon. Since the XPS analysis also showed an increase in chromium oxides, the chromium oxides may be located outside the specified areas, or the layer thickness appears to be smaller than the resolution limit of the EDX analysis (set EDX line scan resolution: 198 nm/point).

To determine whether the oxides have been redistributed by the melt flow convection, or whether the oxide distribution corresponds to the surface topography, Fig. 18 provides an EDX line scan across the specimen surface and a correlating SEM analysis. In contrast to the specimen welded with locally supplied argon (Fig. 13), the chamberless-welded specimen in ambient atmosphere were characterized by a significant seam undercut due to the spatter-induced loss of mass (Section 3.1). Since there was no undercut formation in the corresponding cross section in Fig. 6, it should be noted that Fig. 6 and Fig. 18 represent two different specimens welded with identical parameters.

The EDX analysis revealed a spatial dependence of the element concentration, whereby a noticeably decrease in iron and nickel and an increase in oxygen, manganese and silicon was observed from the seam centre to the seam edge. Although the EDX analysis can be affected by the variation in surface topography due to the seam undercut, this corresponds to the determined differences in oxide layer thickness. It can therefore be assumed that the oxides preferentially segregate in the edge area of the weld seam during the welding process. As described above, this can be a result of the shear-induced forces due to the melt pool convection. In contrast to the clearly formed chevron ripples of the specimen welded with locally supplied argon, a much weaker chevron structure was observed, which also appeared to be symmetrical (Fig. 18, Detail A). The topography of the chevron ripples was found to be rough and characterized by cracks and spalling oxides (Fig. 18, Detail B). This is in line with the described increase in volume of the formed oxides, which can lead to cracking and spalling of the oxides due to the formation of a critical compressive stress [42].

In summary, it can be said that an all-over covering oxide layer with local differences in layer thickness is formed during the welding process in an ambient atmosphere. The

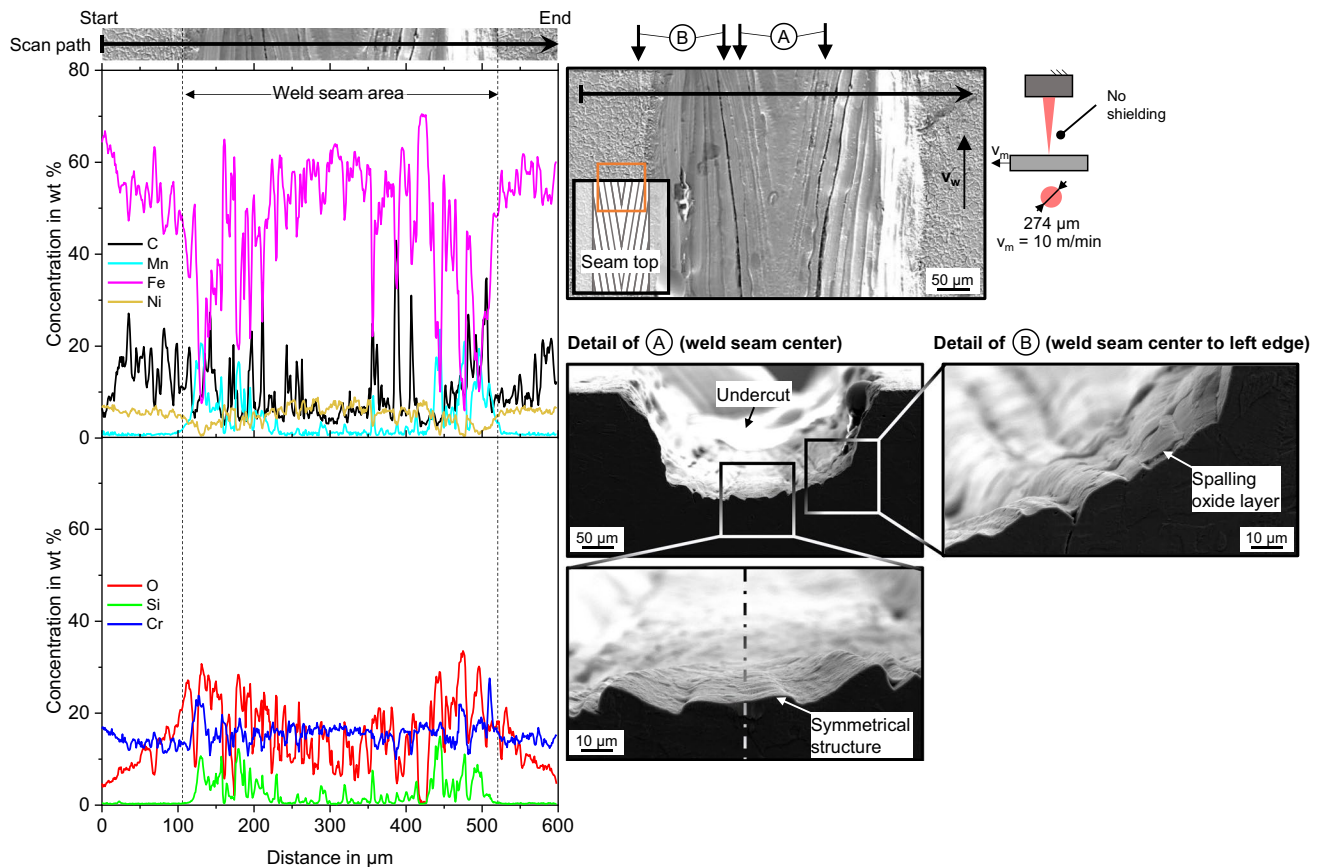


Fig. 18 Surface topography and spatial element distribution of AISI 304 welded chamberless in ambient atmosphere

oxide layer consists mainly of manganese oxide, silicon oxide and a proportion of chromium and iron oxide.

4 Conclusion and outlook

Since there is no significant change in keyhole geometry and dynamics induced by a partial shielding caused by a local argon supply at low flow rates, this paper focuses on the determination of the effect of locally supplied argon on oxide formation, as the oxide growth affects the melt pool dynamics. To qualify the effect of shielding, the experiments are compared to chamber-welded specimens in a global argon atmosphere. As a result of the experiments, following key facts were found (Fig. 19):

4.1 Ambient atmosphere

- Based on the contact of melt and oxygen, an all-over covering oxide layer was formed. The thickness of this layer increased significantly in the seam edge. Inside the oxide layer, cubical structures were stacked on the top of each other. While smaller cubes were settled in the lower part, the largest of them were concentrated on the upper side. These structures were embedded in a lamellar matrix that seems to consist of at least two different elements. The redistribution of oxides was attributed to shear-induced forces due to the melt pool convection. Since the Marangoni convection should be directed centripetal for welding in ambient atmosphere and the effect of the keyhole surrounding flow and the metal vapor induced flow is predominantly for high welding speeds, the effect will be dominated by a resultant of these.
- Using XPS and EDX analyses, the oxide layer was characterized as consisting primarily of oxidized manganese, silicon and parts of chromium and iron. Differences in the concentration of elements within the oxide layer indicate the presence of silicon in the matrix surrounding the cubical structures. This is in line with the oxidation kinetics, whereby the growth of Cr_2O_3 and FeO , among others, form the outer oxides and Fe_2O_3 and SiO_2 , among others, form the inner oxides.
- Based on the loss of mass, the seam may be characterized by a seam undercut (not depicted in Fig. 19). Weakly formed chevron ripples were observed, while the specimen surface was rough and characterized by oxide spalling. This can be attributed to the volume increase of oxides, which can result in a cracking and spalling of them due to the induced compressive stress.

4.2 Partial shielding using local argon supply

- Due to the oxygen shielding of the inert argon, it was not possible to detect an all-over covering oxide layer.

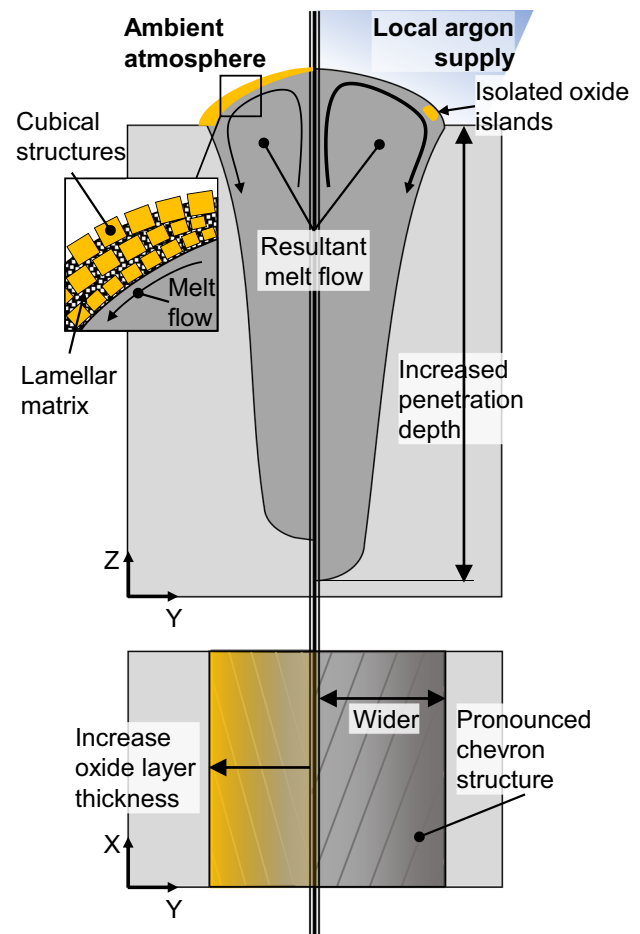


Fig. 19 Effect of partial shielding using locally supplied argon on oxide growth and weld seam geometry

However, it cannot be excluded that an oxide layer was formed, since the local gas supply does not ensure a full-time coverage during the solidification of the seam. In this case, the thickness of this layer should be below the detection limit of the measuring methods used. This is supported by the fact that the imperfect coverage resulted in the formation of oxide islands, which showed an almost comparable elemental composition as the specimen welded in ambient atmosphere. Since these areas were formed at the edge of the seam, this supports the theory of the convection-induced redistribution of oxides. As the temperature coefficient of liquid iron can become negative with a shielding of oxygen, the centrifugal flow direction of the Marangoni flow supports the edge-orientated redistribution and results in a local widening of the seam top.

- In contrast to the decrease in penetration depth of the chamber-welded specimen in a global argon atmosphere, the use of locally supplied argon resulted in an increase in penetration depth. This may be attributed to the flow-sided

blowing of metal vapor resulting in an increase in laser beam transfer efficiency [43, 44].

- As a result of the enhanced convection on the almost free melt pool surface, a pronounced formation of chevron ripples was observed, while the specimen surface was smooth and free of cracks or spalling. The spatial resolved EDX analysis of the specimen top side revealed a correlation between the chemical element concentration and the surface topography. Thus, an increase of the oxidation-relevant elements (Mn, O, Si) was observed on the maxima of the chevron ripples. According to the XPS measurements, this indicates a local increase in oxide layer thickness.

In conclusion, it can be said that the differences in oxide growth led to a significant affected melt pool convection and melt pool dynamics, although the shielding of oxygen also affects spatter formation by influencing the surface tension. Therefore, the fundamental effect of locally supplied argon

at low flow rates (up to 5 l/min) seems to be dominated by the shielding of oxygen. Further investigations will focus on the characterization of the gas penetration within the keyhole, the clarification of the gas-induced melt pool elongation and the analysis of the keyhole dynamics at higher flow rates.

Appendix

This section provides the corresponding high-resolution XPS spectra of Fe $2p_{3/2}$, Cr $2p_{3/2}$ and Mn $2p_{3/2}$ to Section 3.4. Depending on the experimental setup (Section 2.1), Fig. 20, Fig. 21 and Fig. 22 showing the results of the chamber-welded specimen in a global gas atmosphere and Fig. 23, Fig. 24 and Fig. 25 showing the results of the chamberless-welded specimen with locally supplied gas. As chromium is characterized by a multiplet splitting due to unpaired valence electrons [45], the high-resolution XPS spectra of chromium (Fig. 21, Fig. 24) include the related information.

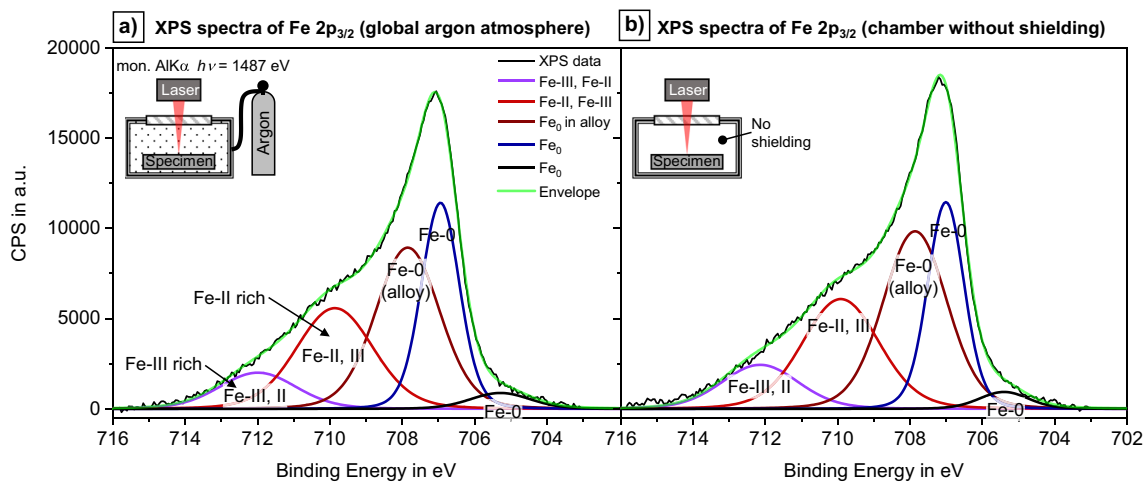


Fig. 20 High-resolution XPS spectra of Fe $2p_{3/2}$: **a** global argon atmosphere, **b** ambient atmosphere inside chamber

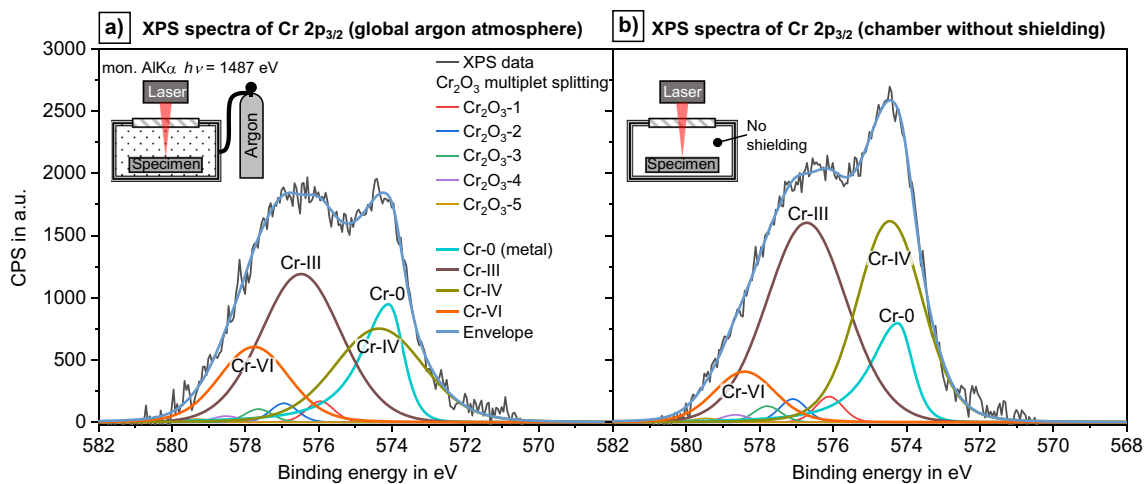


Fig. 21 High-resolution XPS spectra of Cr 2p_{3/2}: **a** global argon atmosphere, **b** ambient atmosphere inside chamber

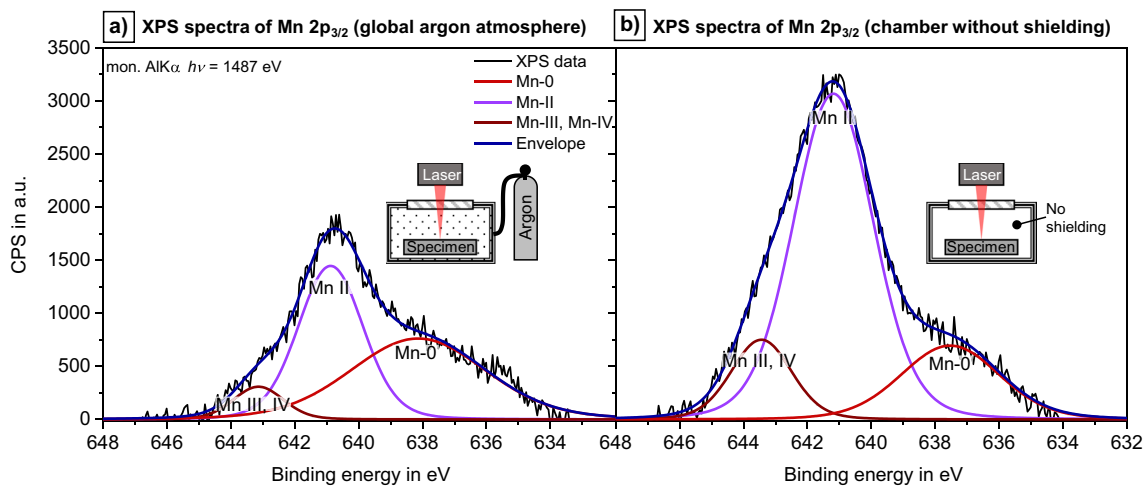


Fig. 22 High-resolution XPS spectra of Mn 2p_{3/2}: **a** global argon atmosphere, **b** ambient atmosphere inside chamber

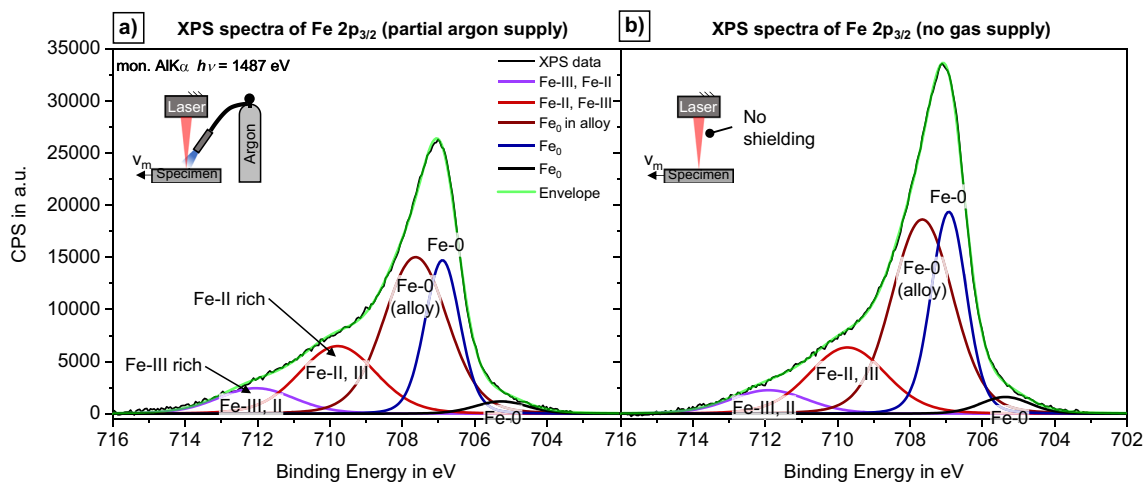


Fig. 23 High-resolution XPS spectra of Fe 2p_{3/2}: **a** locally supplied argon, **b** ambient atmosphere w/o chamber

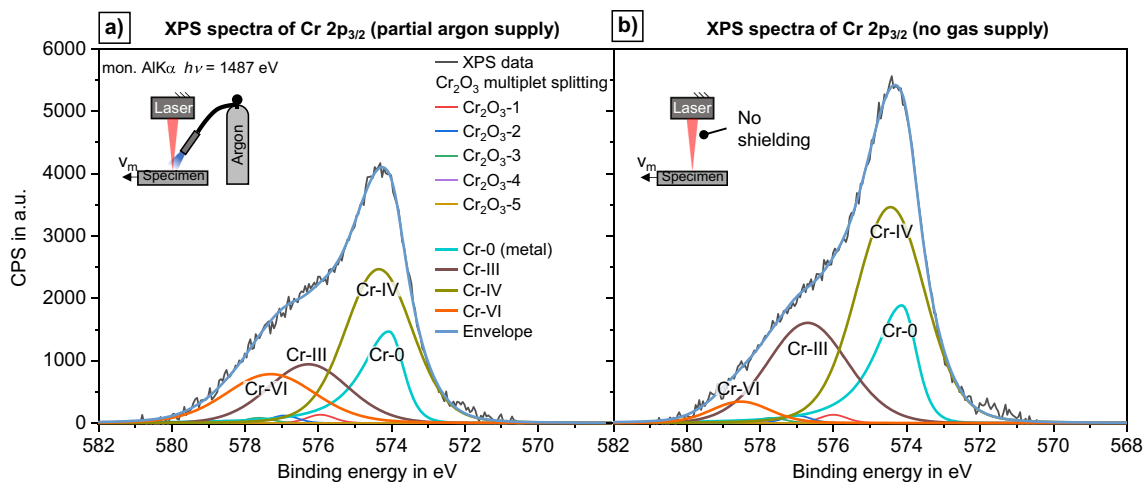


Fig. 24 High-resolution XPS spectra of Cr $2p_{3/2}$: **a** locally supplied argon, **b** ambient atmosphere w/o chamber

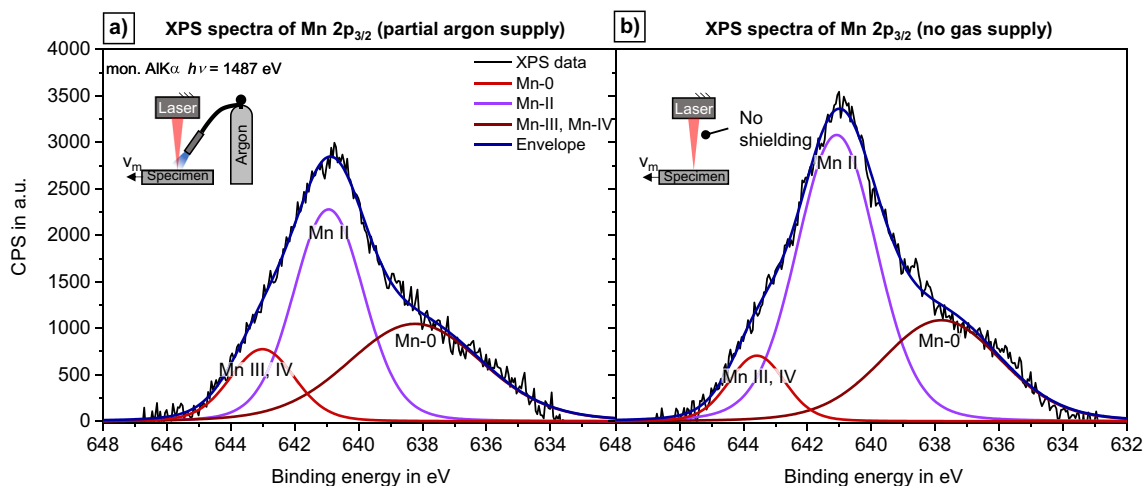


Fig. 25 High-resolution XPS spectra of Mn $2p_{3/2}$: **a** locally supplied argon, **b** ambient atmosphere w/o chamber

Acknowledgements The authors would like to thank Andrea Knauer and Henry Romanus from the Center of Micro- and Nanotechnologies (ZMN) (DFG RI sources reference: RI_00009), a DFG-funded core facility (Grant No. MU 3171/2-1 + 6-1, SCHA 632/19-1 + 27-1, HO 2284/4-1 + 12-1) at TU Ilmenau, for their support with the experiments concerning the XPS, EDX and SEM analyses.

TU Ilmenau thank ESRF – The European Synchrotron for approving the proposal (ME-1580) and the staff of beamline ID19 for their substantial support.

The authors thank the Free State of Thuringia for funding the project “Leistungszentrum InSignA” (2021 FGI 0010) that allowed carrying out the experiments at ESRF.

Funding Open Access funding enabled and organized by Projekt DEAL.

Declarations

Conflict of interest The authors declare no competing interests.

Open Access This article is licensed under a Creative Commons Attribution 4.0 International License, which permits use, sharing, adaptation, distribution and reproduction in any medium or format, as long as you give appropriate credit to the original author(s) and the source, provide a link to the Creative Commons licence, and indicate if changes were made. The images or other third party material in this article are included in the article's Creative Commons licence, unless indicated otherwise in a credit line to the material. If material is not included in the article's Creative Commons licence and your intended use is not permitted by statutory regulation or exceeds the permitted use, you will need to obtain permission directly from the copyright holder. To view a copy of this licence, visit <http://creativecommons.org/licenses/by/4.0/>.

References

- Hügel H, Graf T (2023) Materialbearbeitung mit Laser; Edition Nr. 5. Springer Vieweg Wiesbaden. <https://doi.org/10.1007/978-3-658-41123-7>

2. Kamimuki K, Inoue T, Yasuda K, Muro M, Nakabayashi T, Matsunawa A (2002) Prevention of welding defect by side gas flow and its monitoring method in continuous wave Nd:YAG laser welding. *J Laser Appl* 14:136–145. <https://doi.org/10.2351/1.1493766>
3. Jovic G, Bormann A, Proell J, Boehm S (2019) Laser welding of thin stainless steel parts using modified side-gas application for control of spatter and weld shape. In: Proceedings of International Congress on Laser Advanced Materials Processing (LAMP), Hiroshima, pp 1–7
4. Jovic G, Bormann A, Pröll J, Böhm S (2020) Laser welding with side-gas application and its impact on spatter formation and weld seam shape. *Procedia CIRP* 94:649–654. <https://doi.org/10.1016/j.procir.2020.09.101>
5. Fabbro R, Slimani S, Doudet I, Coste F, Briand F (2006) Experimental study of the dynamical coupling between the induced vapour plume and the melt pool for Nd–Yag CW laser welding. *J Phys D Appl Phys* 39:394–400. <https://doi.org/10.1088/0022-3727/39/2/023>
6. Schmidt L, Hickethier S, Schrickler K, Bergmann JP (2019) Low-spatter high speed welding by use of local shielding gas flows. In: Proceedings of SPIE LASE Conference, vol 10911. <https://doi.org/10.1117/12.2507024>
7. Schmidt L, Schrickler K, Bergmann JP, Hickethier S (2019) Effect of gas flow on spatter formation in deep penetration welding at high welding speeds. In: Proceedings of Lasers in Manufacturing Conference, Munich, pp 1–7
8. Schmidt L, Schrickler K, Bergmann JP, Junger C (2020) Effect of local gas flow in full penetration laser beam welding with high welding speeds. *Applied Sciences*:10, 1867. <https://doi.org/10.3390/app10051867>
9. Beck M (1996) Modellierung des Lasertiefschweißens. PhD Thesis, Universität Stuttgart, Teubner Verlag, Stuttgart
10. Katayama S, Tsukamoto S, Fabbro R (2013) Handbook of laser welding technologies. Woodhead Publishing
11. Schmidt L, Schrickler K, Bergmann J (2021) Experimental and numerical analysis of local gas supplies for spatter reduced high speed laser beam welding. In: Proceedings of Lasers in Manufacturing Conference, Munich, pp 1–10
12. Schmidt L, Schrickler K, Diegel C, Bergmann JP (2022) Effect of local pressure distribution on spatter formation for welding high alloy steel at high welding speeds. *Procedia CIRP* 111:391–396. <https://doi.org/10.1016/j.procir.2022.08.173>
13. Ishide T (1992) High Power YAG laser welded sleeving technology for steam generator tubes in nuclear power plants. In: Proceedings of international conference on laser advanced materials processing--science and applications. Nagaoka, pp 957–962
14. Ono K, Adachi K, Miyamoto I, Inoue T (2002) Influence of oxide film on weld characteristics of mild steel in CO₂ laser welding. *J Laser Appl* 14:73–77. <https://doi.org/10.2351/1.1471563>
15. Fuhrich T, Berger P, Hügel H (2001) Marangoni effect in laser deep penetration welding of steel. *J Laser Appl* 13:178–186. <https://doi.org/10.2351/1.1404412>
16. Naito Y, Mizutani M, Katayama S (2006) Effect of oxygen in ambient atmosphere on penetration characteristics in single yttrium–aluminum–garnet laser and hybrid welding. *J Laser Appl* 18:21–27. <https://doi.org/10.2351/1.2164484>
17. Lu S, Fujii H, Sugiyama H, Tanaka M, Nogi K (2002) Weld penetration and Marangoni convection with oxide fluxes in GTA welding. *Mater Trans* 43:2926–2931
18. Ono K, Adachi K, Katada K, Mishiro M, Miyamoto I, Inoue T (2003) Laser welding phenomena of mild steel with oxide film. Influence of oxide film on high power CO₂ laser welding of mild steel (Report 1), vol 17. *Welding International*, pp 5–11. <https://doi.org/10.1533/wint.2003.3049>
19. Bürgel R, Maier HJ, Niendorf T (2011) *Handbuch Hochtemperatur-Werkstofftechnik: Grundlagen, Werkstoffbeanspruchungen, Hochtemperaturlegierungen und-beschichtungen*. Mit 66 Tabellen; Vieweg+ Teubner
20. Hibiyi T, Morohoshi K, Ozawa S (2010) Oxygen partial pressure dependence of surface tension and its temperature coefficient for metallic melts: a discussion from the viewpoint of solubility and adsorption of oxygen. *J Mater Sci* 45:1986–1992. <https://doi.org/10.1007/s10853-009-4107-2>
21. Fukuyama H, Waseda Y (2008) *High-temperature measurements of materials*, vol 11. Springer Science & Business Media
22. Simon D (2019) Hochtemperaturoxidationsstudien zum Wasserdampfeinfluss auf thermisch wachsende Chromoxidschichten. PhD Thesis, Universität Siegen, Siegen. <https://doi.org/10.25819/ubsi/726>
23. Ricci E, Passerone A (1993) Review: Surface tension and its relations with adsorption, vapourization and surface reactivity of liquid metals. *Mater Sci Eng A* 161:31–40. [https://doi.org/10.1016/0921-5093\(93\)90472-Q](https://doi.org/10.1016/0921-5093(93)90472-Q)
24. Teneva-Kosseva G, Köhne H (2006) Oxidschichtbildung und Materialprobleme metallischer Werkstoffe bei Verbrennungsprozessen mit Heizöl EL. Fakultät für Georessourcen und Materialtechnik
25. Lu S, Fujii H, Nogi K (2004) Marangoni convection and weld shape variations in Ar–O₂ and Ar–CO₂ shielded GTA welding. *Mater Sci Eng A* 380:290–297. <https://doi.org/10.1016/j.msea.2004.05.057>
26. Jun Z, Shi F, Mukai K, Tsukamoto H (1999) Numerical analysis of nitrogen absorption rate accompanied with Marangoni convection in the molten iron under non-inductive stirring condition. *ISIJ International* 39:409–418. <https://doi.org/10.2355/isijinternational.39.409>
27. Keene BJ (1993) Review of data for the surface tension of pure metals. *Int Mater Rev* 38:157–192. <https://doi.org/10.1179/imr.1993.38.4.157>
28. Lancaster JF (1986) *The physics of welding*, 2nd edn. Pergamon Press, pp 1–340
29. Delacroix J, Piluso P, Chikhi N, Asserin O, Borel D, Brosse A, Cadiou S (2022) Measurements of liquid AISI 304L steel density and surface tension, and influence of surface-active elements at high temperatures. *Steel Res Int* 93:2100624. <https://doi.org/10.1002/srin.202100624>
30. Kaplan A (1994) Modellrechnung und numerische simulation von absorption, Wärmeleitung und Strömung des Laser-Tiefschweißens. PhD Thesis, TU Wien, Wien
31. Tanaka M, Lowke JJ (2007) Predictions of weld pool profiles using plasma physics. *J Phys D Appl Phys* 40:R1. <https://doi.org/10.1088/0022-3727/40/1/R01>
32. Hirashima N, Choo RTC, Toguri JM, Mukai K (1995) The effect of surface movements on nitrogen mass transfer in liquid iron. *Metall Mater Trans B* 26:971–980. <https://doi.org/10.1007/BF02654098>
33. Rack A, Garcia-Moreno F, Schmitt C, Betz O, Cecilia A, Ershov A, Rack T, Banhart J, Zabler S (2010) On the possibilities of hard X-ray imaging with high spatio-temporal resolution using polychromatic synchrotron radiation. *J Xray Sci Technol* 18:429–441. <https://doi.org/10.3233/XST-2010-0273>
34. Schindelin J, Arganda-Carreras I, Frise E, Kaynig V, Longair M, Pietzsch T, Preibisch S, Rueden C, Saalfeld S, Schmid B et al (2012) Fiji: an open-source platform for biological-image analysis. *Nat Methods* 9:676–682. <https://doi.org/10.1038/nmeth.2019>
35. Matsunawa A, Mizutani M, Katayama S, Seto N (2003) Porosity formation mechanism and its prevention in laser welding. *Weld Int* 17:431–437. <https://doi.org/10.1533/wint.2003.3138>

36. Fabbro R (2010) Melt pool and keyhole behaviour analysis for deep penetration laser welding. *J Phys D Appl Phys* 43:445501. <https://doi.org/10.1088/0022-3727/43/44/445501>
37. Robertson SM, Kaplan AFH, Frostevarg J (2021) Material ejection attempts during laser keyhole welding. *J Manuf Process* 67:91–100. <https://doi.org/10.1016/j.jmapro.2021.04.052>
38. Van der Heide P (2011) X-ray photoelectron spectroscopy: an introduction to principles and practices. John Wiley & Sons. <https://doi.org/10.1002/9781118162897>
39. Hüfner S (2013) Photoelectron spectroscopy: principles and applications. Springer Science & Business Media
40. Herty CH, Fitterer GR (1931) New manganese-silicon alloys for the deoxidation of steel, vol 3081. United States Bureau of Mines
41. Dowden J, Kapadia P (1996) A mathematical model of the chevron-like wave pattern on a weld piece. In: Proceedings of the international congress on applications of lasers & electro-optics, pp B96–B105. <https://doi.org/10.2351/1.5059030>
42. Xu C, Gao W (2000) Pilling-Bedworth ratio for oxidation of alloys. *Mater Res Innov* 3:231–235. <https://doi.org/10.1007/s100190050008>
43. Greses J, Hilton PA, Barlow CY, Steen WM (2004) Plume attenuation under high power Nd:yttrium–aluminum–garnet laser welding. *J Laser Appl* 16:9–15. <https://doi.org/10.2351/1.1642636>
44. Jose G, Claire YB, Paul AH, William MS (2003) Effects of different gas environments on CO₂ and Nd:YAG laser welding process efficiencies. In: Proceedings of the Proc. SPIE, Osaka, pp 257–262. <https://doi.org/10.1117/12.486500>
45. Allen GC, Tucker PM (1976) Multiplet splitting of X-ray photoelectron lines of chromium complexes. The effect of covalency on the 2p core level spin-orbit separation. *Inorg Chim Acta* 16:41–45. [https://doi.org/10.1016/S0020-1693\(00\)91689-X](https://doi.org/10.1016/S0020-1693(00)91689-X)

Publisher's Note Springer Nature remains neutral with regard to jurisdictional claims in published maps and institutional affiliations.